ARTICLE IN PRESS

Available online at www.sciencedirect.com

SCIENCE DIRECT®

ELSEVIER

Progress in Biophysics and Molecular Biology ▮ (▮▮▮▮) ▮▮▮–▮▮▮

Progress in Biophysics & Molecular Biology

www.elsevier.com/locate/pbiomolbio

Review

Macroscopic optical mapping of excitation in cardiac cell networks with ultra-high spatiotemporal resolution

Emilia Entcheva[a,b,*], Harold Bien[a]

[a]*Department of Biomedical Engineering, Stony Brook University, HSC T18-030, Stony Brook, NY 11794-8181, USA*
[b]*Department of Physiology and Biophysics, Stony Brook University, Stony Brook, NY 11794, USA*

Abstract

Optical mapping of cardiac excitation using voltage- and calcium-sensitive dyes has allowed a unique view into excitation wave dynamics, and facilitated scientific discovery in the cardiovascular field. At the same time, the structural complexity of the native heart has prompted the design of simplified experimental models of cardiac tissue using cultured cell networks. Such reduced experimental models form a natural bridge between single cells and tissue/organ level experimental systems to validate and advance theoretical concepts of cardiac propagation and arrhythmias. Macroscopic mapping (over $>1\,cm^2$ areas) of transmembrane potentials and intracellular calcium in these cultured cardiomyocyte networks is a relatively new development and lags behind whole heart imaging due to technical challenges. In this paper, we review the state-of-the-art technology in the field, examine specific aspects of such measurements and outline a rational system design approach. Particular attention is given to recent developments of sensitive detectors allowing mapping with ultra-high spatiotemporal resolution (>5 megapixels/s). Their interfacing with computer platforms to match the high data throughput, unique for this new generation of detectors, is discussed here. This critical review is intended to guide basic science researchers in assembling optical mapping systems for optimized macroscopic imaging with high resolution in a cultured cell setting. The tools and analysis are not limited to cardiac preparations, but are applicable for dynamic fluorescence imaging in networks of any excitable media.

Keywords: Optical mapping; Cultured cells; Fluorescent probes; Calcium; Transmembrane potentials

Contents

*Corresponding author. Department of Biomedical Engineering, Stony Brook University, HSC T18-030, Stony Brook, NY 11794-8181, USA. Tel.: +1 631 444 2368; fax: +1 631 444 6646.
E-mail address: emilia.entcheva@sunysb.edu (E. Entcheva).

0079-6107/$ - see front matter
doi:10.1016/j.pbiomolbio.2005.10.003

1. Introduction

Excitation waves are complex spatiotemporal phenomena encoding essential functional information for healthy and diseased excitable tissue, including the heart. The visualization of these waves in live tissue was facilitated by the introduction of fast fluorescent probes for changes in transmembrane voltage and intracellular calcium concentration, and by the development of appropriate optical techniques to image their response (Salama and Morad, 1976; Grinvald et al., 1977; Ross et al., 1977; Morad and Salama, 1979; Gross et al., 1986; Ehrenberg et al., 1987; Tsien, 1983; Grynkiewicz et al., 1985a). Since then, *optical mapping* (multi-site fluorescence measurements with high temporal and spatial resolution) has made possible the direct experimental testing of theoretical concepts about cardiac arrhythmias, cardioversion and electrical excitation in the heart. Optical mapping in culture-grown monolayers or patterns of myocytes allows the study of cellular processes in their natural context, avoiding some of the deficiencies associated with the two extremes: isolated cells or whole heart measurements. It permits the true dissection of propagation phenomena and direct links to computational models of the same by controlled local or global alterations of structural and functional properties—a feature not readily available in whole heart or tissue preparations. Thus, cultured cardiomyocyte networks form a natural bridge between single cell and whole heart studies in cardiac electrophysiology.

Optical *microscopic mapping in cardiomyocyte cultures* was pioneered by Rohr, Fast and Kleber at the University of Bern, employing patterned cell growth (Rohr et al., 1991) and custom-developed imaging system using a fluorescence microscope, photodiodes and optical fibers (Rohr and Salzberg, 1994; Rohr and Kucera, 1998). In a series of elegant optical mapping studies, this group and their collaborators addressed questions of load mismatch in structurally complex cell network architectures (Fast and Kleber, 1993, 1995a, b; Rohr et al., 1997), cell-level polarization patterns in response to external electrical fields in cardioversion and defibrillation (Fast et al., 1998, 2004; Gillis et al., 1996, 2000; Tung and Kleber, 2000; Fast and Ideker, 2000), micro-reentrant phenomena in slow propagation conditions (Kucera et al., 1998; Rohr and Kucera, 1997), etc.

Understanding cell network behavior at the *macroscopic scale* and the study of phenomena underlying dangerous cardiac arrhythmias required the extension of this imaging approach to accommodate a larger field of view (FOV). Signature reentrant waves, believed to be at the core of cardiac arrhythmias, are macroscopic spatiotemporal phenomena, taking place over a spatial scale that is linked to the wavelength for propagation ($\lambda_w = \theta w$, where θ is the wave's conduction velocity and w signifies the duration of the events of interest—action potentials or calcium transients). For typical values of θ and w, the spatial scale of interest is in the centimeter range, thus requiring a matching FOV in that range. Due to technical difficulties and limitations of optical imaging at low magnification in low light levels, the transition from micro- to macroscale mapping in monolayer cell cultures is not trivial, i.e. is not as simple as changing an objective.

The first attempts at *macroscale mapping of cardiac electromechanics in cultured cells* (voltage or calcium waves) originated in three laboratories. Bub, Shrier and Glass at McGill University (Bub et al., 1998, 2002, 2003) used a charge-coupled device (CCD)-based system to track the dynamics of spontaneous and induced spiral waves as a function of cell density and age in cultured embryonic chick cells. Tung lab at Johns Hopkins University (Entcheva et al., 2000, 2004b; Iravanian et al., 2003) developed a contact fluorescence imaging (CFI) approach combining photodiodes and fiber optics to study anatomical and functional reentry in neonatal rat cultures. Sarvazyan lab at Texas Tech University (Arutunyan et al., 2001, 2002) used a confocal system to assess calcium dynamics in reperfusion injury in cultured cell networks with a geometrically defined

ischemic zone. In these first attempts at macroscopic mapping in cardiac cell monolayers, the overall spatiotemporal resolution was insufficient—typically the focus was on one of the aspects—either good temporal or good spatial resolution.

Mechanistic understanding of the spatiotemporal phenomena underlying cardiac arrhythmias calls for both—micro- and macroscale imaging, preferably done simultaneously and using appropriate acquisition rates. The requirement for combined macro/micro-examination is of particular importance for phenomena occurring at fine spatial scales or in a heterogeneous setting. Examples include the activity at the core of a macroscopic spiral wave, cell-level phenomena during macroscopic wave meandering and wavebreaks in fibrillation-like conditions, coupling and propagation between discrete structures of cell populations (stem cells and myocytes, for example). The most interesting and clinically relevant excitation phenomena (such as associated with polymorphic ventricular tachycardia and fibrillation) are by definition unpredictable in space–time; therefore, it is close to impossible to a priori localize the zone of interest (for detailed micro-mapping) within the macro-image. A brute-force approach can be used alternatively—a single *detector with ultra-high spatiotemporal resolution* to conduct micro-level (sub-cellular) imaging within a macroscale FOV. To date, no such tools have been described; and, indeed, current *macroscopic* optical mapping has never approached the spatial resolution common for computer models of propagation.

Specific questions concerning optical imaging of spatiotemporal phenomena at the macroscale ($>1\,cm^2$) in cell culture preparations have not been addressed in the numerous optical mapping reviews and technical papers published in the field over the last 30 years (Cohen et al., 1978; Morad and Salama, 1979; Salama, 1988; Salzberg, 1989; Rohr and Salzberg, 1994; Baxter et al., 1997; Bullen et al., 1997; Rohr and Kucera, 1998; Wu et al., 1998; Wu and Cohen, 1999; Bullen and Saggau, 1999; Tominaga et al., 2000, 2001; Grinvald et al., 2001; Sakai and Kamino, 2001; Efimov et al., 2004; Grinvald and Hildesheim, 2004). With very few exceptions (Rohr and Salzberg, 1994; Rohr and Kucera, 1998; Bullen and Saggau, 1999), most of the above papers have dealt with tissue-level measurements of electrical activity in cardiac and brain preparations, not with cell monolayers.

We have come to the realization that there are unique challenges for macroscopic (low magnification) optical mapping in cultured cell monolayers, and this paper aims at providing the missing perspective. More specifically, this review outlines a theoretical framework where the choice of imaging detector is made based on a "shortest distance" from an "ideal" optical mapping system. In this context, we critically review the newest detector technology with ultra-high spatiotemporal resolution (>5 megapixels/s) and present the first macro-mapping and micro-mapping data at such high resolution. We discuss new technical issues (detector–computer interface), arising only in conjunction with the very high information throughput in this new class of photodetectors.

The structure of the review is as follows: (1) challenges of low magnification fluorescence imaging and suitable optical arrangements for cell monolayers; (2) issues concerning the use and calibration of fluorescent labels; (3) illumination solutions for cell culture imaging; (4) review of state-of-the-art photodetectors with ultra-high spatiotemporal resolution and appropriate sensitivity for cell culture mapping; (5) new technical challenges of very high data throughput, and review of the capabilities of current computer technology to meet them; (6) theoretical analysis for rational design of a "minimal" and an "ideal" imaging systems, and evaluation of the available detector technology in terms of "closeness" to the ideal target.

2. Challenges of low magnification (macroscopic) optical measurements

2.1. Why is it difficult to map fluorescence at low magnification?

Intuitively, low magnification is expected to provide larger pixel area to collect light from and to improve optical signals. However, this notion is not quite correct—fluorescence imaging at low magnification is adversely affected by the quality of the optics available. In addition, by increasing the number of pixels as the FOV grows to maintain the spatial resolution within acceptable limits, the imaged area per pixel is not substantially larger.

Current high-power microscope lenses (objectives), which have evolved to aid scientific discovery, feature impressive light-collecting ability (LCA), usually quantified by their numerical aperture (NA). NA indicates

the ability of a lens to effectively collect diffracted rays of light, and provide high-resolution power. $NA = n\sin(\alpha/2)$, where n is the index of refraction of the medium and α the maximum solid angle of acceptance of light at the optical axis.

Macroscale mapping of electrical propagation is needed to visualize spatiotemporal patterns occurring over a large area (1 cm^2 or more). At the same time, the imaging area of the current photodetector technology has practical size limitations—the chip size is close to or even smaller than the desired FOV. This requires operation at low magnification. Commercially available objectives in this range ($<2\times$) have very poor light-gathering ability (very low NA). Typically below $10\times$, it is rare for an objective lens to have $NA > 0.3$ (compare this to $NA = 1.4$ for a good $60\times$ objective).

There are a couple of factors preventing the achievement of high NA in low magnification objectives:

(1) *Medium of operation*: High NA lenses achieve $NA > 1$ by operating in media different from air ($n = 1$), such as water ($n = 1.33$) or oil ($n = 1.55$). Macroscopic imaging cannot benefit from these higher index of refraction media because of practical reasons—large separation between the sample and the objective (i.e. large working distance (WD)).
(2) *Working distance*: Most of the low magnification lenses cover a large FOV and, therefore, operate at large WDs. The latter means large focal lengths (f), which translate into low NA, since for simple lenses the NA is inversely proportional to the focal length ($NA \propto f^{-1}$).
(3) *Lens size*: A way to compensate for the compromised NA is to increase the lens diameter (d), because ($NA \propto d$). However, in a standard microscope setting, there are limits to this diameter increase. For macroscopic lenses outside the microscope, a large diameter is possible, yet it is technically challenging to achieve a high surface curvature needed for a high angle of acceptance in these big lenses.

As a result, high NA lenses for macroscopic imaging are rare. Lenses with suitable characteristics can be found in photography—the so-called "fast" lenses, featuring very low F-number (note that $NA = 0.5n/\#F$) and used in very low light levels. The lowest $\#F$ (highest NA) in a commercially produced compound lens is 0.7 (made by Zeiss 50 mm $F/0.7$, not currently available). Such a lens would have $NA = 0.71$, if operated at infinity. There are currently available large diameter fast lenses made by Canon (50 mm $F/0.95$), Navitar

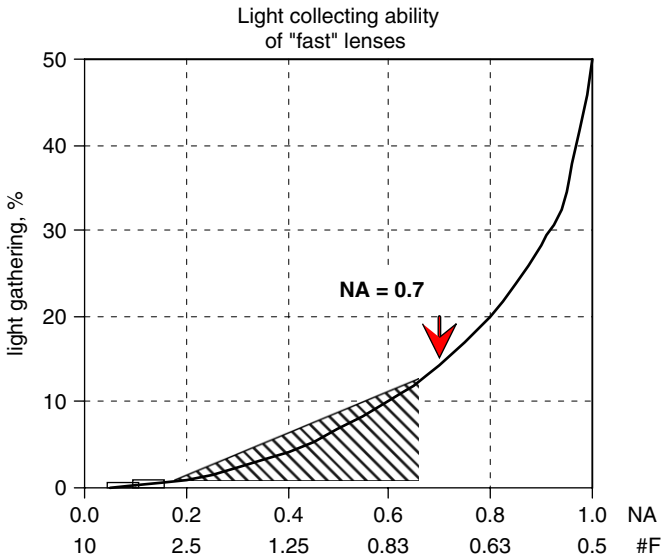

Fig. 1. Light-collecting ability of low magnification imaging lenses is a nonlinear function of their NA ($\#F$). Light-gathering ability is theoretically calculated as a percent collected light from the total light from a radially emitting point source, as a function of the numerical aperture (NA) or the $\#F$ of a lens. The shaded region shows the range for the currently manufactured "fast" lenses.

(DO-5095 50 mm $F/0.95$), Leica (Noctilux 50 mm $F/1$), Nikon (Nikkor 35 mm $F/1.4$, Nikkor 105 mm $F/2$), etc., which cover focal distances from 35 to 105 mm, and $\#F$ from 0.9 to 2.0 (corresponding NA = 0.55–0.25).

Fig. 1 presents the theoretically determined LCA of lenses in the NA range (0.05–1), operating in air. Calculations according to Eq. (1) (based on pure geometrical considerations) are presented as a percent collected light (volume fraction) from the total emitted light by an ideal light-radiating point source (the total luminous flux is represented by the volume of a sphere) using standard formulae (Zwillinger, 1996, p. 315). Note that the currently available "fast" lenses cover only the low LCA range. For example, the fastest lens ever made offers nine times better light-gathering ability than a reasonably fast lens with $\#F$ of 2:

$$\mathrm{LCA} = \frac{1 - \sqrt{1 - (\mathrm{NA})^2}}{2}. \tag{1}$$

In addition to poor LCA, low NA lenses lead to deterioration in spatial resolution, δx, of the signal as per the Rayleigh criterion, Eq. (2) (Murphy, 2001). For example, for emitted light with wavelength $\lambda = 0.6\,\mu\mathrm{m}$, and a lens having low NA = 0.1, the limit of resolution (7.3 μm according to Eq. (2)) is considerably worse than the wavelength-determined limit:

$$\delta x = \frac{1.22\lambda}{\mathrm{NA}}. \tag{2}$$

2.2. Why do cultured cell systems present more challenges than whole heart measurements?

Fluorescence signals are depth integrated; thus, the challenges of macroscale mapping increase in inverse proportion to the thickness of the imaged preparation. Upon illumination of the sample, excitation of the fluorescent dye molecules takes place over a certain tissue volume (depth of 0.3–1.3 mm below the surface; Knisley, 1995; Girouard et al., 1996; Baxter et al., 2001). Depending on the local tissue structure, absorption properties and scattering, emitted light is also collected from a volume, rather than a surface plane. In

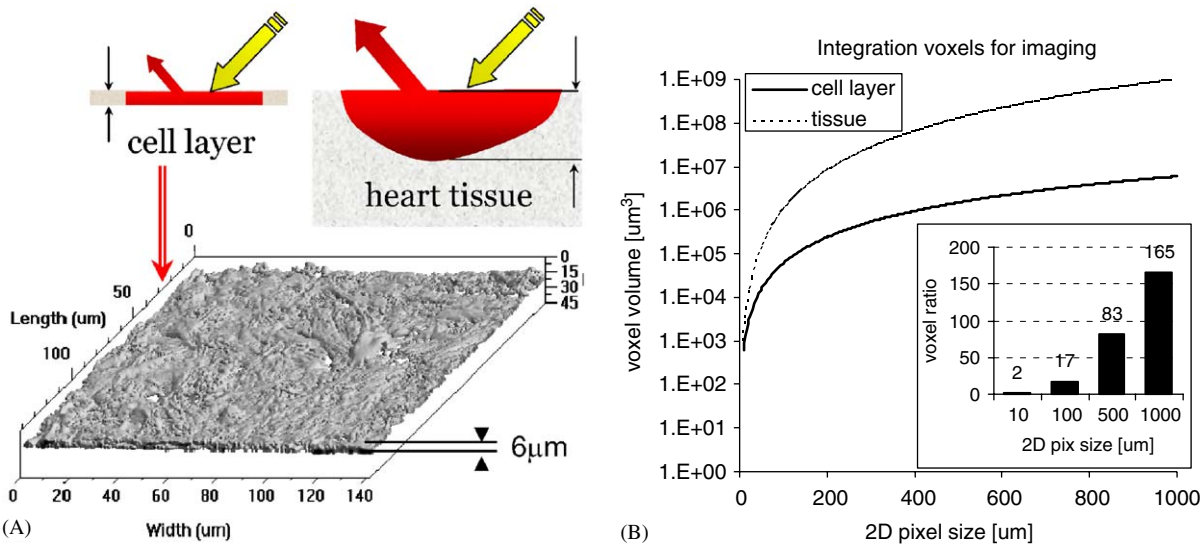

Fig. 2. Fluorescence signals are volume integrated, resulting in differences when imaging cardiac tissue vs. cell monolayers. (A) Schematic representation of the integration depth issue when imaging thin cell layers vs. cardiac tissue. On the bottom, an actual 3D reconstruction of a cultured cardiomyocyte layer. The image is based on multiple confocal images of the cytoskeleton (F-actin), total thickness 6 μm. (B) The graph presents the voxel volume (μm^3) for a range of square pixels (10–1000 μm); a cell height of 6 μm is used for the cell monolayer. The inset shows selected ratios of voxel volumes between the two preparations, after the data have been corrected with the empirical exponential functions by Baxter et al. The voxels seen in tissue become 165 times larger than seen in monolayers for 1 mm pixels.

contrast, in cultured cardiomyocyte networks, the thickness of the whole sample is only 5–10 μm, as assessed by confocal imaging and three-dimensional (3D) volume reconstruction of the cytoskeleton (*F*-actin was labeled) in our lab, Fig. 2A, or as measured by atomic force microscopy (Domke et al., 1999). This is at least an order of magnitude thinner than the low limit for the depth of field (DOF) of relevant lenses (Inoue and Spring, 1997, p. 48); thus, the monolayer height becomes the limiting factor for the amount of collected light in this type of imaging, regardless of the employed optics. Fig. 2B presents the sample volume (or imaging voxel) difference between tissue and a cell layer, as a function of the spatial resolution (2D pixel size) during imaging. The graph does not take into account the impact of the optics quality via DOF, i.e. the values for tissue measurements might be overestimated for cases where high NA lenses are used, which may somewhat restrict the effective depth of integration. The inset shows selected volume ratios, after a correction function has been applied for the depth contribution of different layers, as derived empirically by Baxter et al. (2001). This difference alone can contribute to 2–165 times larger signals in tissue vs. monolayers, as the spatial resolution varies from 10 μm to 1 mm/pixel. The implication is that a corresponding >100 times change in photodetector sensitivity or an overall improvement of all system components might be needed in order to adapt them from tissue-level imaging to mapping in cell monolayers at the same magnification.

2.3. Viable optical arrangements for mapping in cultured cell systems

There are three possible solutions to obtain useful signals at low magnification optical mapping in thin cell preparations. These include: (1) the use of high NA large diameter single lenses; (2) tandem-lens (TL) assembly optics; and (3) lens-less transfer of the image to the photodetector using versions of CFI, Fig. 3.

Using a single "fast" lens in front of the detector is a simple solution. However, high NA low magnification lenses typically have a pronounced vignetting effect (loss of light away from the optical axis), and introduce spherical aberrations when operated at small distances. Furthermore, "fast" lenses perform at their maximum NA (corresponding to the indicated #*F*) when focused at infinity. At finite WDs to the sample (usually a couple of centimeters), the effective NA is lower.

The TL configuration (Ratzlaff and Grinvald, 1991) combines two "fast" lenses, focused at infinity and facing each other, to guarantee high NA performance at practical WDs to the sample, and to facilitate epi-fluorescence measurements using identical optical pathways for the excitation light and for the emitted light. The sample is placed at the back focal plane of the smaller lens (L1); the camera is at the back focal plane of

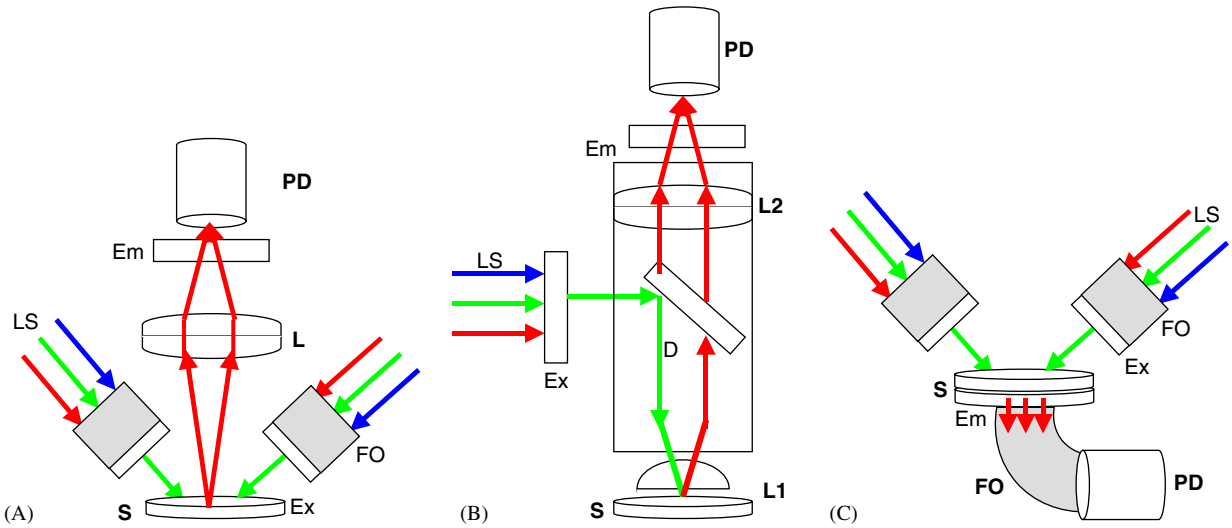

Fig. 3. Optical solutions for low magnification imaging in cell monolayers: (A) single high NA lens; (B) tandem-lens assembly; (C) contact fluorescence imaging (CFI) setup. The following components are depicted: S, sample; PD, photodetector; LS, light source; Em and Ex, emission and excitation filters; D, dichroic mirror; L, lens; L1, L2, objective and imaging lenses for TL assembly; FO, fiber optics.

the larger diameter lens (L2). The ratio of the focal lengths (f_{L2}/f_{L1}) determines the magnification of the system. The effective LCA of the TL system is affected by the distance between the lenses to some extent, since the infinity focus does not result in perfectly parallel rays of light from L1 to L2. The actual WD (L1 back surface to the sample) for a true TL configuration is limited by the particular standard lens chosen. The flange back focal length (distance from the L1 mounting thread to the sample) is 12.5 mm for CS-mount lenses, 17.5 mm for *C*-mount lenses and 46.5 mm for standard *F*-mount (35 mm SLR) lenses. Hence, SLR lenses are preferred in a TL assembly. A disadvantage of the TL approach is the increase in the number of glass–air interfaces. This is undesirable because of the decrease in contrast these interfaces might cause due to reflections. Sophisticated compound lenses usually have >6 elements, and any small reflection (0.1–4%) at each of the more than 12 interfaces/lens can contribute to loss in light transmission and image contrast.

Finally, because of the difficulties in finding/designing high NA optics in the low magnification range, it is logical to attempt to directly project the image on the surface of the detector, minimizing separation and avoiding optical relay lenses. It is not practical, however, to have the surface of the photodetector chip in physical contact with the experimental sample, even through a glass coverslip, because of the obvious risk of damage. A practical alternative is offered by an optical fiber coupler—optical fibers arranged in a tight bundle of desired geometry, placed between the experimental sample and the photodetectors. There are standard optical fibers with a reasonably good NA = 0.5 (corresponding to #*F* of 1). We demonstrated this idea by a custom-designed CFI system (Entcheva et al., 2000, 2004b), where each fiber was linked to an individual photodiode. Such CFI system has the following features: (1) provides a fixed $1\times$ magnification; (2) takes advantage of the planar nature of a cultured cell monolayer; it has no equivalent of a focal plane; (3) solves some of the vignetting and spherical aberration problems and glass–air interface issues characteristic for lens-based approaches, because the light transfer is uniform across the FOV and fully determined by the individual optical fiber properties. Among the limitations of the CFI optical solution are the restriction to only transillumination type of excitation light delivery and the inability for easy change of spatial resolution/magnification.

3. Use and calibration of fluorescent probes for excitation

Two classes of fast-response fluorescent indicators have been developed in the last 30 years suitable for dynamic measurements of cardiac electromechanics—voltage-sensitive (or potentiometric) dyes and calcium-sensitive dyes. For action potentials measurements, the styryl dyes (di-4-ANEPPS, di-8-ANEPPS and RH-237), excitable by visible light, are most widely used for optical mapping in myocyte cultures (Windisch et al., 1985; Loew et al., 1992; Rohr and Salzberg, 1994). The fluorescence response of di-8-ANEPPS has been shown to change linearly with transmembrane potential in simultaneous optical and patch-clamp recordings (Bullen and Saggau, 1999). Because of the "all-or-nothing" nature of the action potential (constant amplitude), calibration and conversion into millivolts is rarely conducted. Instead, the relative change in fluorescence ($\Delta F/F$) is typically reported. A drawback of the currently used potentiometric dyes is their poor signal-to-noise ratio (SNR)—for macroscopic measurements in cultured cells, the fluorescence change is typically $<5\%$. There is a clear need for voltage-sensitive dyes with improved response, and such efforts are underway (Efimov et al., 2004).

Along with action potentials, cycling in intracellular calcium is of great interest for better understanding of arrhythmogenesis. Calcium transients are not perceived merely as events unidirectionally controlled by the action potentials. Processes associated with cardiac calcium handling (triggered or spontaneous calcium release, and calcium uptake) can affect the timecourse and stability of the membrane potential (Chudin et al., 1999; Eisner et al., 2000; Guatimosim et al., 2002). Optical measurements of intracellular calcium are facilitated in cell monolayers compared to tissue-level mapping because of the lack of extensive motion artifacts and no need for mechanical immobilization.

Fluorescent indicators for intracellular calcium (Takahashi et al., 1999) offer a substantially better SNR (up to a 1000-fold change in fluorescence upon Ca^{2+} presence) than the currently available voltage-sensitive dyes. They have evolved to cover a spectrum of excitation wavelengths (UV and visible light) and a range of calcium affinity (different k_d constants). For example, the UV-excitable indicator Fura-2AM can be used to distinguish very low levels (<50 nM) because of its high Ca^{2+} affinity. This makes it the probe of choice for measuring

subtle alterations in diastolic calcium. At the other end of the spectrum are the very low-affinity probes ($k_d > 1\,\mu M$), such as Fluo-4FF, Fluo-5N and Rhod-FF, which can be used if a large dynamic range (DR) of calcium concentrations is expected. These indicators are likely to operate in their linear range when physiological systolic calcium levels are encountered; thus, they introduce minimum distortion and/or artificial prolongation of the transients due to saturation, the tradeoff being a mediocre SNR (Fast et al., 2004).

Common problems in the interpretation of optical measurements of intracellular calcium for most Ca^{2+} indicators are dye loading (compartmentalization and uptake by mitochondria and sarcoplasmic reticulum, incomplete hydrolysis, etc.) and in vivo calibration. The ratiometric calcium dyes (Fura-2 and Indo-1) exhibit different emission and/or excitation spectra for the free and Ca^{2+}-bound form. This feature allows ratiometric measurements, i.e. forming a ratio after fluorescence is measured at two different wavelengths—excitation ratio for Fura-2 and emission ratio for Indo-1. Such measurements are less sensitive to variations due to dye loading, illumination and other artifacts, and make possible the conversion into Ca^{2+} concentration. A method for two-point Fura-2 calibration was proposed by Grynkiewicz et al. (1985b) using values at zero and maximum calcium. Zero Ca^{2+} can be achieved after cell treatment with a calcium scavenger (such as EGTA), while saturating intracellular Ca^{2+} concentrations can be reached by a membrane-compromising agent (such as ionomycin), equilibrating intra- and extracellular Ca^{2+} concentrations. Typically, determining the fluorescence at maximum Ca^{2+} is problematic (Yin et al., 2004). Various calibration approaches have been attempted, including metabolic inhibition to minimize the active processes counteracting ion equilibration (Frampton et al., 1991) and BDM treatment to prevent hypercontracture (Cheung et al., 1989), but with variable success.

A distinct difference between optical mapping in intact hearts and cell culture preparations is the method of dye labeling. In whole hearts, typically the dyes are delivered via coronary system perfusion, whereas in monolayers the cells are bathed in dye solution with usually higher concentration than used in tissue preparations. As a result, the dye has a higher chance of getting trapped in the extracellular matrix, which may contribute to increased or uneven background fluorescence. Additionally, for intracellular probes, dye entrapment in various organelles seems to be more pronounced for cell monolayers. These differences in dye delivery may partially contribute to higher sensitivity to phototoxic damage (via release of reactive oxygen species) in cell monolayers vs. tissue. In the latter, healthier cells from the sub-surface layers have been suggested to play a protective role serving as a potential anti-oxidant source (Salama, 1988).

The intimate understanding of normal and pathological processes in cardiac electromechanics ultimately requires simultaneous mapping of voltage and calcium. Previous dual dye measurements have used separation of the two signals by excitation, by emission or both. Dye pairs, successfully used in simultaneous measurements of action potentials and intracellular calcium include: di-2-ANEPEQ and calcium green (Bullen and Saggau, 1998); di-4-ANEPPS and Indo-1 (Laurita and Singal, 2001); di-4-ANEPPS and Fluo-4 (Johnson et al., 1999); RH-237 and Rhod-2 (Choi and Salama, 2000); RH-237 and Fluo-3/4 (Fast and Ideker, 2000; Kong et al., 2003). In some of these experiments, the dye spectra and their overlap were of primary interest; thus, measurements were not co-localized in space and/or time (Kong et al., 2003; Johnson et al., 1999). Our lab has had success with dual imaging in cultured myocyte layers with no crosstalk using di-8-ANEPPS and Fura-2, where measurements require a broad excitation and optical separation of emission.

4. Illumination solutions for the cultured cell setting

Due to the transparent flat nature of the cultured cell preparation, two modes of illumination are possible. In *transillumination*, the detector and the light source are at opposite sides of the sample, while in *epi-illumination* mode the delivery of light and the collection of light are on the same side of the sample. Transillumination is a simple solution, typical for work with cultured cells (in fact, is the only solution compatible with CFI), and does not require beamsplitters. It can be accomplished by one or more light guides brought to the sample at some angle (avoiding direct coupling into the detector). Problems associated with transillumination are: achieving consistent positioning from experiment to experiment, uniform sample illumination and effective filtering of the delivered light by the emission filter, since interference emission filters perform best when the rays are perpendicular to their surface. Uneven illumination combined with the small

response of the voltage-sensitive dyes can result in a substantially reduced DR and can obscure the signals of interest.

Epi-illumination allows the delivery of excitation light through an identical optical path as the collection of the emitted light. This mode of illumination is best served by the TL assembly, where a dichroic mirror (beamsplitter) between the two lenses selectively reflects lower wavelengths (in the excitation light range) toward the sample and passes higher wavelengths (in the emitted light range) from the sample to the detector. In epi-illumination, the characteristics of the objective lens (its NA) factor in twice in the quality of the acquired image—via the efficiency of light delivery and the efficiency of light collection.

The intensity of the excitation light has to be optimized carefully. As low as $6\,\mathrm{mW/cm^2}$ (achievable by a couple of ultra-bright light-emitting diodes) has been shown to be sufficient for macroscopic fluorescence imaging (Entcheva et al., 2004b). Increasing excitation light intensity will increase the intensity of the emitted light, and hence will improve the SNR. However, there is an upper limit—cell monolayers are particularly sensitive to dye photobleaching and phototoxicity, inducible by long exposures to a particularly intense excitation light.

From the traditional light sources, xenon (Xe) arc lamps and quartz–tungsten halogen (QTH) lamps are most often used in conjunction with cell culture imaging. They offer a continuous spectrum over the excitation range suitable for the current voltage-sensitive dyes and some of the calcium-sensitive dyes (400–700 nm) (Lackowicz, 1999). The QTH lamps cannot provide UV illumination required for a class of Ca^{2+} sensitive dyes, and have a limited output below 450 nm. Semiconductor-generated illumination (ultra-bright LEDs and laser diodes) has only recently become a viable alternative (Entcheva et al., 2004b), offering a wide range of wavelengths, including those of interest for fluorescence measurements in living cells. LED illumination is a more cost-effective, energy efficient, portable and flexible solution. Computer (TTL-level) control is possible for easy on/off switching and also for high-frequency light modulation. This feature can provide the means for synchronized (lock-in) detection and/or for fast wavelength switching, thus allowing excitation ratio imaging or dual label imaging. High intensity LED illumination appropriate for fluorescence measurements in cultured cells is currently offered by a number of companies—from simple lower current LEDs by Nichia to higher current higher intensity LED lamps by Lumileds.

5. State-of-the-art detector technology

The most important component of an optical mapping system is the detector. There are currently a limited number of suitable detectors in use or of potential interest for fast multi-site optical measurements in cardiac preparations. These include: photodiode arrays (PDAs), CCD cameras and complementary metal-oxide semiconductor (CMOS) cameras. Since cell cultured systems have special requirements for increased sensitivity (as compared to tissue measurements), two derivative versions of cameras with increased sensitivity are also of interest: (1) on-chip electron multiplication CCDs (or EMCCDs); and (2) intensified camera systems (I-CCD/CMOS). EMCCDs rival in sensitivity the older technological solution, where a camera (CCD or CMOS) is coupled to an intensifier.

Choosing a detector system is a multi-parameter optimization problem. We have mapped the five categories of detectors mentioned above onto a three-parameter space, including temporal resolution, spatial resolution and sensitivity (Fig. 4). This qualitative diagram reflects the trends in the current day detectors; it is only to be used as a crude detector selection guide. *Spatial resolution* is the number of pixels in a detector. *Temporal resolution* is defined as frames per second (fps), thus for practical purposes detectors with high spatial resolution appear much slower regardless of their per-pixel rate. Sensitivity is used here in a utility sense—the ability of a detector to produce useful signal at each pixel under optimal illumination conditions. The obvious pitfalls of such definition are that many important factors are not taken into account to equalize the performance metrics—mainly, pixels are not normalized by area.

In more strict technical terms, the *sensitivity* of a detector is directly affected by three classes of noise: *dark current noise* (Δn_D), *shot noise* (Δn_S) and *readout noise* (Δn_R) (Wu et al., 1998; Tominaga et al., 2000):

$$\text{noise} = \sqrt{\Delta n_D^2 + \Delta n_S^2 + \Delta n_R^2}. \tag{3}$$

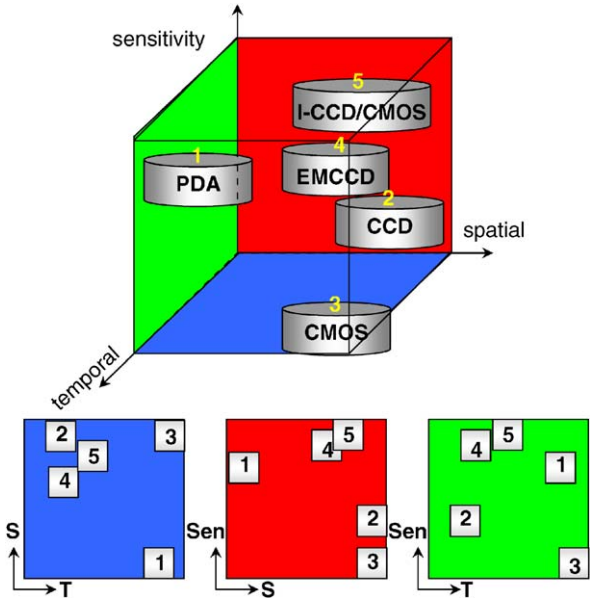

Fig. 4. Current photodetector technology mapped onto a 3D parameter space of temporal resolution (*T*), spatial resolution (*S*) and sensitivity (Sen). Represented are (1) PDA, (2) CCD, (3) CMOS, (4) EMCCD and (5) I-CCD/CMOS detectors. See text for details.

The *limit of detection* of a system (and the lower bound of its effective DR) is determined by the intersection of the floor noise—a combination of Δn_D and Δn_R—and the shot noise (a function of the signal intensity). For imaging in cell monolayers with barely detectable fluorescence signals, special attention should be paid to reduce the floor noise. The readout noise starts contributing significantly when the per-pixel rate (clock rate) of the detector becomes too high (exceeds 5 MHz, for example), which is the case for most ultra-high-resolution detectors. At the same time, the higher the clock/acquisition rates, the smaller the dark current noise (due to thermal and other factors); hence, multi-pixel cameras have lower Δn_D than PDAs. The shot noise reflects random variations in the signal itself due to the quantum nature of light, and scales up with the square root of the signal intensity. For example, 10 times higher intensity of the signal will result in about three times better SNR during imaging ($10/\sqrt{10}$). The DR of the detector is particularly important for measurements with voltage-sensitive dyes which have relatively high background fluorescence but a very small dynamic change in fluorescence. The upper bound of the effective DR of a detector is determined by the pixel *well depth/capacity* (maximum per-pixel charge before saturation). For practical reasons, large well depth (resulting in a higher effective DR) is synonymous with a large light-gathering area, i.e. large pixels. The bit resolution of the photodetector (8–16 bit, typically) is informative in terms of theoretical DR, only if the floor noise of the system is known and a fixed bin size is considered. For all practical purposes, the effective DR (as discussed above) is more instructive for the performance of the detector. Another important parameter to consider is the quantum efficiency (QE) of the detector, indicating what portion of the photons reaching the detector surface is converted into a measurable signal. For very low light levels (such as in cell monolayers), high acquisition rates and small pixels, it is not uncommon that <10 photons hit a pixel per frame. For a QE of 50%, this will result in SNR of only about 1.3 (Andor Technology, 2003).

For measurements in cell culture, PDAs are most widely used, including a commercially available 16×16 PDA from Hamamatsu and custom-made PDAs with up to 500 detectors from WuTech (Wu and Cohen, 1999). Flexible spatial arrangements can be obtained by custom-developed systems where tightly packed optical fibers are coupled to individual photodiodes (similar to the WuTech solution) (Rohr and Kucera, 1998; Entcheva et al., 2000; Iravanian et al., 2003). Currently, PDAs dominate optical mapping in cell culture because they produce signals with good SNR, and provide good temporal resolution. In addition, the PDAs can be operated in AC-coupled regime and background "bias" can be subtracted to stretch the changes in

fluorescence across the full DR. This feature is particularly important for voltage-sensitive dyes with high resting level fluorescence and little dynamic changes. PDA's high sensitivity is largely a result of the big pixels—they integrate fluorescence over areas of about 1 mm^2 or more in CFI regime (Entcheva et al., 2000), while for a comparable magnification camera systems rarely exceed pixel size of 10^{-2} mm^2 without binning (spatial averaging of pixels). The limited spatial resolution is the main disadvantage of the PDA systems, since it becomes impractical and cost-ineffective to expand such arrays beyond 500 photodiodes.

CCD systems, which dominate whole heart optical mapping (Baxter et al., 1997; Gray et al., 1998; Witkowski et al., 1998b; Lin et al., 1997) are currently not widely used for cell culture imaging. The main benefit of CCD camera imaging is the higher spatial resolution. Yet, in the extremely low light level conditions typical for cell monolayers, current day CCDs fail to produce useful signals on a single pixel level at high rates, despite their lower dark current noise. The much smaller pixel size (compared to PDAs) is the major difference. Spatial binning can improve the image, but resolution is lost. In addition, the increased number of pixels per frame (from a typical 256 pix for a PDA to $>10{,}000$ pix for a CCD) comes with a cost—reduced temporal resolution or increased readout noise. On the market, there are currently very few CCDs which attempt to combine high spatial and high temporal resolution, yet yield useful image. The manufacturers typically optimize one or the other. Successful examples of use of CCD detectors for imaging cell culture typically involve the better performing calcium-sensitive dyes (Bub et al., 1998). Yet the acquisition rates in these measurements have been sub-optimal. Our own experience includes signals from the RedShirt 80×80 camera, SciMedia MiCAM, pco1600 and Dalsa 128. The tests were not performed at the same light conditions and optics, and the cameras vary in resolution, thus is not straightforward to rank their performance.

CMOS imagers have been usually omitted or briefly mentioned in most reviews on optical mapping in excitable tissue. However, they seem to meet the demands for combined high spatial and temporal resolution. The speedup is achieved by higher level of parallelism compared to CCDs—the serial readout in the CCDs is substituted with individually addressable pixels and per-pixel electronics in the CMOS. The tradeoff is a significantly lower sensitivity compared to CCDs. This drawback can be overcome by using a very large well depth (pixels as big as $25 \times 25\,\mu m$). Technological innovations in the geometry of the CMOS photoelements also include reduction in electrical surface leakage, which reduces the dark current noise. We have tested several of these new CMOS cameras—the Silicon Imaging 1024F (1024×1024 pix), SciMedia Ultima 100×100 pixels and pco1200 (1280×1024 pix). At high illumination levels and optimized optics, all three cameras have a potential as photodetectors in cell culture. The CMOS cameras are, in general, inexpensive or less expensive than CCDs. However, the specialized large pixel CMOS cameras, with added memory and processing capabilities, are currently forming a sub-category and are selling for a rather high price. While the CCD technology might be approaching its performance limits, especially in the temporal domain, CMOS technology is on the rise and is expected to improve further by maximizing the fraction of the light-collecting area on the chip using back-illumination or other methods. Because of technological compatibility with traditional electronics, CMOS sensors can also incorporate image processing as part of the sensor, which is expected to make them more competitive than CCDs in optical mapping.

Ways to improve the performance of the cameras include back-illumination, cooling and addition of intensifiers. Back-illumination is used to improve the QE of the cameras. It involves thinning (etching away) the crystalline silicon substrate along the path traveled by the emitted photons toward the sensing elements, which reduces the loss of photons due to absorption, hence increases QE. Cooling reduces the thermal noise—a major contributor to the dark current noise. When the detectors are operated at high clock rates (low exposure times), improvements in SNR by cooling are not substantial. Image intensifiers improve sensitivity but are generally perceived as noise-introducing and possibly resolution-limiting components in the optical system. They require special handling because of their proneness to damage by direct light. Yet they are widely used (and needed) for extremely low light level conditions, such as single molecule detection studies. The weak fluorescent signals from a single layer of cells fall into the category of very low light conditions. An intensified CCD system (two-stage intensifier) has been used before in optical mapping of the whole heart (Witkowski et al., 1998a). We have used a Generation II single-stage intensified MTI-DAGE camera at 60 fps with a spatial resolution 320×240 pix to image voltage and calcium signals in cultured cells (Bien et al., 2003; Entcheva et al., 2004a) and Generation III intensified pco1200 CMOS camera at 200 fps.

In image intensifiers, first a photocathode converts image photons into e^-, then 1–3 multi-channel plates (MCP) guide the e^- multiplication in small channels under high voltage, after which the resultant e^- cloud is steered across a small spatial gap toward a phosphorous screen, which converts the multiplied e^- back into photons (see Chapter 8 in Inoue and Spring, 1997; Molecular Expressions, 2005 for additional information). A fiber optic guide (1:1 or tapered as needed) accomplishes the final transfer of the image at the phosphor screen onto the camera chip. The temporal resolution of an intensifier is limited by the life time of the particular phosphor used—the common P43 has a life time of about 1 ms, while P46, 47 have a sub-microsecond life time. The spatial resolution is mostly limited by the size of the electron cloud per channel, reaching the phosphor screen; current Generation III intensifiers offer at least 64 line-pairs/mm (analogous to 15.6 μm effective pixels at $1\times$ magnification). The QE in intensified systems refers to the percentage of the entry photons that are transformed into electrons reaching the MCP; it is as high as 50% for Generation III intensifiers without a protective MCP films. When combined with a fast CCD or CMOS, intensified system can provide enough sensitivity for imaging in cell culture.

A more modern concept for increasing sensitivity is used in the cameras with on-chip electron multiplication, known as EMCCDs (Denvir and Conroy, 2003; Robbins and Hadwen, 2003) or charge-carrier multiplication cameras (Hynecek, 2001; Hynecek and Nishiwaki, 2003). These are all-solid-state devices, unlike the intensifiers described above; they utilize the process of impact ionization (an avalanche process) before the acquired values are converted into voltage. A fully chip-incorporated "gain register" provides electron multiplication in a serial process involving the application of high electric fields. The major EMCCD benefits include: (1) lower readout noise at higher speeds (which is a common problem for fast CCDs); (2) lower multiplicative noise (involved in the amplification of the original signal plus the shot noise); (3) improved QE compared to intensifiers; (4) minimized image artifacts and distortion (as sometimes seen in intensified systems). A drawback is the decrease in the DR at high gains. Some new EMCCDs, among which Andor Ixon 512 and Roper 512 back-illuminated cameras, show promise as high-resolution cameras for cell monolayers. However, the EMCCDs currently are rarely driven at >10 MHz/pixel, which limits the combined increase in spatial and temporal resolution; chips with higher clock speeds are under development. The EMCCDs face even higher limitations (than CCDs) in terms of achievable per-pixel rates (and hence—improvement in temporal resolution), because switching of higher electric fields is needed at high gains. Nevertheless, in the long run these photodetectors show the highest promise for fast imaging at very low light levels, encountered in mapping of voltage and calcium waves in cultured cells.

6. High data throughput challenges

With the need to image at a higher spatial resolution while maintaining useful speeds and FOV, the data throughput increases to colossal proportions, not encountered in previous systems for whole heart imaging. This requires special technical solutions at the camera–computer interface. To illustrate the disparate scales of data throughput, in Table 1, we compare the data streams for several typical optical mapping systems, based on commercially available detectors. The data throughput (in Mbytes/s or MBs) is calculated as the product of temporal and spatial resolution, scaled by the DR (1 or 2 bytes/pixel). The observed values span over more than three orders of magnitude in desired bandwidth: 0.6–1310 MBs.

A common solution to the high data flow problem is the addition of on board memory for immediate data storage and data transfer to disk afterwards. This memory can be incorporated directly in the camera head (CamRAM) or can be added to the specialized camera–computer interface boards, known as frame grabbers. For example, 4 GB on board memory for the pco CMOS camera (used ingenuously by special data packing) allows the recording of 78 s of data at 200 fps for VGA-equivalent region of interest. Such a solution is not practical for continuous recordings >5 min in duration due to prohibitive RAM size required. Alternatively, data can be streamed directly to the RAM of the computer via Direct Memory Access, where the process will be limited by the expandability of the computer RAM. For 32 bit processor systems the limit is 4 GB. But 64 bit memory-addressing schemes and ultimately 64 bit processor systems will be able to offer RAM capacity well in excess of the 4 GB limit, and might become the solution of choice for direct data streaming in the future.

Table 1
Comparison of data throughput produced by some optical mapping systems in use

	System description	Data throughput	Bit resolution (bit)	Temporal resolution	Spatial resolution (pixel size)
1	Hamamatsu 16 × 16 PDA at 1 kHz	0.6 MBs	> 8	1000 fps	16 × 16 pix (950 μm/pix)
2	Hamamatsu 16 × 16 PDA at 10 kHz	6 MBs	> 8	10,000 fps	16 × 16 pix (950 μm/pix)
3	WuTech 500 PDA at 5 kHz	5 MBs	> 8	5000 fps	500 pix ([a])
4	Andor/Roper EmCCD 512 at 30 fps	3.9 MBs	> 8	30 fps	512 × 512 pix (16 μm/pix)
5	Andor EmCCD 128 at 400 fps	13 MBs	> 8	400 fps	128 × 128 pix (24 μm/pix)
6	Dalsa CCD 128, 8 bit, at 1000 fps	16.4 MBs	8	1000 fps	128 × 128 pix (16 μm/pix)
7	RedShirt CCD 256 at 100 fps	13 MBs	> 8	100 fps	256 × 256 pix (26 μm/pix)
8	RedShirt CCD 80 at 2000 fps	25.6 MBs	> 8	2000 fps	80 × 80 pix (24 μm/pix)
9	Cooke CCD 1600 × 1200 at 33 fps	126 MBs	> 8	33 fps	1600 × 1200 pix (7.4 μm/pix)
10	SciMedia CMOS Ultima 100 × 100 at 1000 fps	20 MBs	> 8	1000 fps	100 × 100 pix (100 μm/pix)
11	SciMedia CMOS Ultima 100 × 100 at 10,000 fps	200 MBs	> 8	10,000 fps	100 × 100 pix (100 μm/pix)
12	pco CMOS 1280 × 1024 at 200 fps, VGA region of interest (ROI)	123 MBs	> 8	200 fps	640 × 480 pix (12 μm/pix)
13	pco CMOS 1280 × 1024 at 500 fps	1310 MBs	> 8	500 pfs	1280 × 1024 pix (12 μm/pix)
14	*"Ideal" Detector* at $\delta t = 10\,\mu m$, $\delta x = 5$ ms (200 fps), FOV = 2 cm (based on wavelength = 0.1 s∗20 cm/s)	*1.6 GBs*	> 8	200 pfs	2000 × 2000 pix (10 μm/pix)

[a]Pixel size depends on the fiber size used in CFI, typically is > 500 μm/pix.

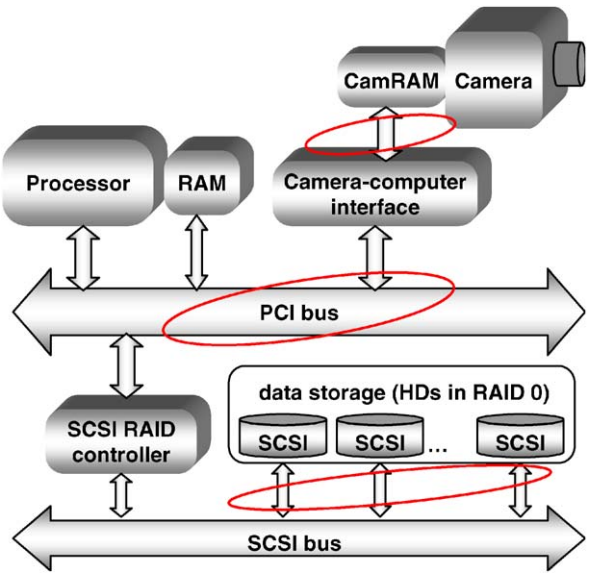

Fig. 5. Camera–computer interface: bottlenecks in data transfer and data storage (circled in red).

Can a sustained recording speed of > 150 MBs (required by the ultra-high-resolution cameras) be achieved with the current computer technology? A diagram of the relevant camera–computer interface components is given in Fig. 5, where the data transfer bottlenecks are circled in red. These include: (1) the camera–computer

interface capacity; (2) the internal computer bus bandwidth; and (3) the writing speed to the hard drives (HDs).

The data transfer from the camera to a computer is done via a standard or specialized *camera–computer interface*. Frame grabbers represent such specialized interface boards. Table 2 lists fast standard interfaces and the sustained rates of data transfer that they can support. While Firewire and USB2, which are routinely included in most current computers, can meet the needs of lower resolution cameras, only the newer CameraLink (from the specialized interfaces) can support real time data transfer for the ultra-high-resolution cameras (National Semiconductor, 2005). CameraLink is a data transfer protocol using a general purpose interface known as Low Voltage Differential Signaling (PULNix America, 2005). Several companies, including National Instruments and Coreco Imaging offer CameraLink frame grabbers. At the high end of data throughput (see Table 1), even this high speed standard fails. Future developments using 10 Gbit Ethernet interface have the potential to virtually lift the restrictions in bandwidth at the camera–computer interface.

The second bottleneck (Fig. 5) is the maximum data transfer rate supported by the internal *communication bus* in the computer. Most frame grabbers use the Peripheral Component Interconnect bus (known as the PCI bus). Several versions of the PCI bus are in use today, offering different speeds (Table 3) (PCI-SIG Group, 2005; Wilen et al., 2002). The current standard, 32 bit PCI (sustained rates <100 MBs), is incapable to meet the demands of ultra-high-resolution cameras. Only higher-end desktop computers today offer 64 bit versions of the PCI bus. The new standard, PCI-Express, was introduced in 2002, and desktop computers incorporating this very high bandwidth bus just start to appear on the market (end of 2004).

A bottleneck in Fig. 5, which is most difficult to overcome in order to transfer data in real time for ultra-high-resolution cameras, is the speed of *writing to a storage device* (HD). Common standardized protocols for data transfer to HDs include ATA, SATA, small computer system interface (SCSI) and fiber channel (FC) (LSI Logic Corporation, 2005; Intel Corporation, 2005). ATA combines several parallel bus protocols for communication with HDs, and offers a capacity of up to 100 MBs sustained rate. It was recently replaced with a serial, faster and easier to configure version, SATA, which features up to 150 MBs data transfer rates. Configuring a system with ATA or SATA devices is relatively inexpensive, but the available HDs compatible with this protocol can only reach sustained writing speed of about 50 MBs. This is insufficient to use them in real time systems with ultra-high-resolution cameras (see Table 1). A more robust option is the SCSI parallel protocol. The current standard Ultra 320 SCSI bus can sustain up to 320 MBs. The SCSI HDs are more intelligent devices (require less processor intervention) and operate at 10,000 or 15,000 rpm, which translates

Table 2
Camera–computer interfaces for fast data transfer

Detector–computer interface	Sustained speed (MBs)
USB2	40–50
IEEE1394b (Firewire)	50–60
1 Gbit Ethernet	128
CameraLink	>200–500
10 Gbit Ethernet	1280

Table 3
Computer parallel bus speeds

Parallel bus types (PCI)	Burst speed (MBs)	Sustained speed (MBs)
32 bits PCI	133	<100
64 bits 66 MHz PCI	530	>200
64 bits 133 MHz PCI-X	>1000	>300
64 bits PCI-Express (PCI-E)	300–15,000	250–4000

into 60–70 MBs sustained writing rates per drive (speeds not achievable in SATA drives). Additional attraction of the SCSI solution for storage is extensibility. Up to 15 SCSI drives can be connected to a single-channel SCSI controller, supporting redundant array of inexpensive drives (RAID) (Katz et al., 1989; Patterson et al., 1988). In particular, RAID-0 regime allows for very high data transfer (limited by the SCSI bus speed—320 MBs) by "stripping" the data to multiple SCSI HDs in parallel operation (no redundancy). FC drives can also be used in a similar RAID-0 configuration. Such parallel HD operation seems to provide the best solution for handling the high data throughput in real time (Fig. 5). The tradeoff for the better speeds obtained in RAID-0 regime is the reduced safety in data storage and increased risk for failure as the number of parallel drives increases. Therefore, this solution has to be used only for real time data streaming but not for permanent storage.

7. Theoretical considerations for an ideal optical mapping system

Having discussed the capabilities of current imaging technology, in this section, we pose the question—how close are we to what can be defined as a "minimal" and as an "ideal" optical mapping system? The theoretical considerations below provide the basis for answering this question.

7.1. Minimum requirements

The constraints in choosing the parameters for an optical mapping system are set by the phenomenon/object characteristics, O. Important characteristics of the phenomenon/object under observation to be considered for imaging include: (1) the minimum duration of an event of interest (w), which sets the limits for temporal sampling; (2) the minimum radius of wavefront curvature before failure of propagation, setting the limits for the spatial resolution in 2D and 3D; and (3) the conduction velocity (θ), known to be a function of the radius of curvature of the wavefront (Fast and Kleber, 1997). The object-determined constraints are

$$O = \{w_{\min}, r_{\min}, \theta(r)\}. \tag{4}$$

The optical system parameters to be optimized are reduced to an essential sub-set S, including: (1) temporal resolution (δt), spatial resolution (δx) and number of pixels (N) to secure a desired FOV. It is assumed that for isotropic tissue, δx and n will be applicable for both spatial axes x and y:

$$S = \{\delta t, \delta x, N\}. \tag{5}$$

The parameters in S are linked via the mapped FOV as follows:

$$\mathrm{FOV} = N\delta x, \tag{6}$$

$$\mathrm{FOV} \geqslant k\delta t\theta, \quad k \geqslant 2. \tag{7}$$

Eq. (7) links space and time, and expresses the requirement to have at least two isochrones (lines connecting points with the same time of activation) within a chosen FOV. Combining Eqs. (6) and (7), one can derive the following relationship, linking the three original parameters of the system, S, so that they form a constant-θ 3D surface:

$$\frac{N\delta x}{\delta t} \geqslant k\theta. \tag{8}$$

Furthermore, considering the most demanding case for temporal sampling, which occurs for the shortest observable event of interest, $w_{\min}$, and the most demanding case for spatial sampling, which occurs for the critical wavelength curvature, $r_{\min}$, we obtain

$$k\delta t \leqslant w_{\min}, \tag{9}$$

$$k\delta x \leqslant r_{\min}. \tag{10}$$

From Eqs. (7) to (9), a 3D hyperbolic surface is obtained that encompasses the parameter space for an optical system capable of capturing propagation in a cardiac preparation with known typical and minimum

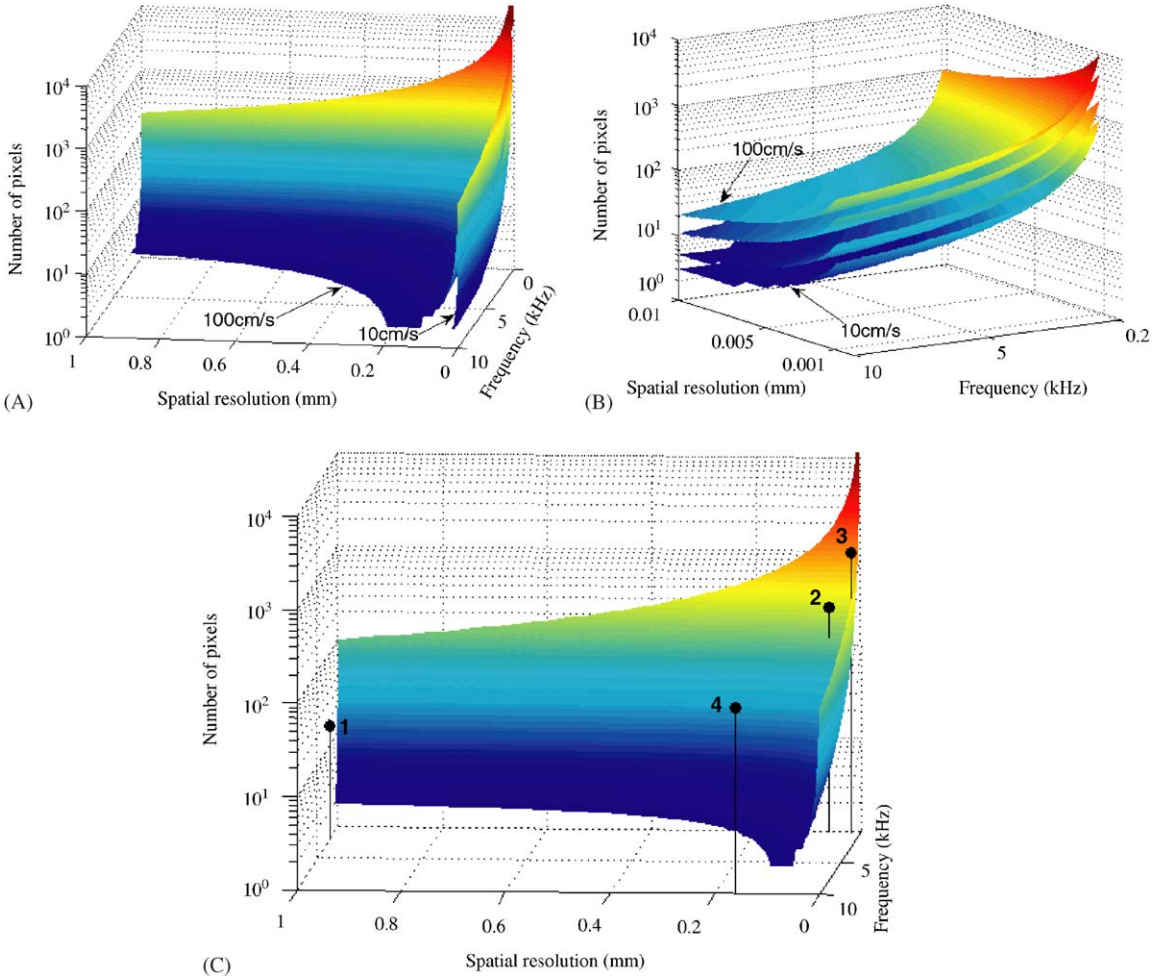

Fig. 6. Minimal requirements 3D surface for an optical mapping system. The three axes include: spatial resolution, temporal resolution (frequency) and total number of pixels. (A) View at the minimum requirements surface for imaging samples with conduction velocities of 10 and 100 cm/s; (B) a closer view at the constant-θ 3D surfaces in the range of relevant spatial and temporal resolution; (C) the minimum requirement 3D surface for $\theta = 50$ cm/s plotted along four current detectors (black dots). The selected detectors are: (1) 16×16 PDA at 1 kHz; (2) 512×512 CCD at 0.1 kHz; (3) 1200×1024 CMOS at 0.2 kHz; and (4) 100×100 CMOS at 10 kHz—all satisfied the minimum requirements (appear on the upper side of the surface).

characteristics. The parameters of an optical mapping system have to fall on the upper side of the plotted minimum parameter surface, satisfying the Nyquist sampling criterion in space and time:

$$N\delta x \geqslant k\delta t\theta_{\text{typ}} \geqslant w_{\min}\theta_{\text{typ}}, \quad k = 2. \tag{11}$$

Examples of such hyperbolic constant-θ 3D surface, satisfying Eq. (11), are shown in Fig. 6 for variable conduction velocities, assuming $w_{\min}$ of 20 ms. It is seen that most of the current detectors in use do meet these minimal criteria (are on the upper side of the 3D surfaces). The spatiotemporal characteristics of the sample under observation can vary, i.e. the duration of the events of interest can vary according to the restitution (frequency-dependent) properties of the tissue. The conduction velocity can also exhibit restitution-dependent variations, as well as changes due to the wavefront curvature (Fast and Kleber, 1997). The choice of specific parameters for optical mapping has to take into account the worst-case scenario for these sample characteristics.

7.2. Spatiotemporal resolution for an ideal mapping system

Registering the existence of a propagating wave (using the minimum requirements above) is a much less restrictive condition than requiring the full capture of spatiotemporal events of cardiac propagation in their complexity. This new, more restrictive, set of requirements is discussed below.

The *physical limits* for optical mapping are determined by the properties of the fluorescent dyes available. For the voltage-sensitive dyes, these limits are $\delta x_{phys} > 0.5\,\mu m$ (optical limits of resolution) and $\delta t_{phys} > 5\,\mu s$ ($f < 200\,kHz$), due to the dye response time limitations (Grinvald and Hildesheim, 2004). Note that imperfect optics can make these limitations more stringent.

Temporal resolution, δt: By physiological constraints, cardiac electrical events are not instantaneous in time. Cardiac activation includes a very fast upstroke but always followed by some refractory period, during which a new event is not possible. If the goal of optical mapping is to elucidate spatiotemporal phenomena, but not necessarily preserve the exact morphology of the activation events, then it is sufficient to consider the highest possible frequency of events. For mammals, this frequency varies between 0.5 and 12 Hz in normal rhythm (Noujaim et al., 2004). Ventricular fibrillation (VF) admittedly represents the high-frequency limit for activation. Previous reports for VF frequency fall mostly in the 8–20 Hz range (Choi et al., 2002; Berenfeld et al., 2000; Zaitsev et al., 2000; Gray et al., 1998; Witkowski et al., 1998b; Wu et al., 2002), but for small mammals (mice) frequencies up to 50 Hz can be reached. Considering conservatively, the highest frequency of events to be twice that high limit—i.e. 100 Hz ($\delta t = 10\,ms$), we need a minimum sampling frequency (maximum time step, δt) of 200 Hz ($\delta t_{max} = 5\,ms$). For the proposed temporal resolution (200 Hz), when a minimum FOV of 1 cm and a maximum θ of 30 cm/s for a cultured cell system are considered, at least six isochrones in the FOV would be guaranteed. It has to be understood, that this temporal resolution assures that no event would be missed, but it does not guarantee reconstruction of the exact temporal profile of the events.

Spatial resolution, δx: While the temporal limits of electrical events of interest (action potentials and calcium transients) are well studied and understood, the spatial limits relevant to propagation are much harder to define. What is the smallest space in which discrete events affecting propagation can take place? This question goes at the heart of the philosophical debate about continuous vs. discrete nature of cardiac propagation.

On the one hand, cells in the heart are very well coupled (Jongsma and Wilders, 2000), and for practical purposes, heart tissue is viewed as a syncytium. In this representation, the lower limit for the spatial scale of events of interest should be functionally linked to the wavelength, most likely through a critical geometrical parameter for propagation—the *radius of critical curvature* before propagation failure. Knowledge of this sample characteristic is informative in setting the lowest spatial resolution for the mapping system. Winfree (1997, 1998) examined the scale of events, viewing the heart as a classical reaction-diffusion system. His analysis of the radius of critical curvature yielded a number in the range of 300 μm for a system satisfying the continuum requirement, i.e. having a diffusion coefficient $D > 1\,mm^2/s$ (Winfree, 1998). This critical curvature of the wavefront has been probed experimentally in studies dealing with point stimulation, propagation through an isthmus or spiral wave propagation (Knisley and Hill, 1995; Cabo et al., 1994), well summarized in a review by Fast and Kleber (1997). These experimental results showed that the radius of the critical curvature can be as low as 100 μm, but the exact number is still not known.

On the other hand, the discrete nature of cardiac propagation events has been exemplified in theoretical (Spach and Heidlage, 1995; Spach et al., 1998, 2000) and experimental studies. Discrete propagation is more relevant to pathological conditions, which are of interest in these optical mapping studies. Imaging at progressively smaller spatial scales reveals that complex spatial patterns can occur at the micro-scale (Kucera et al., 1998; Rohr et al., 1998; Sharifov et al., 2004), or even sub-cellularly (Cheng et al., 1996; Ishida et al., 1999; Kurebayashi et al., 2004) when calcium concentration is concerned. Slowly propagating calcium waves (conduction velocities 40–100 μm/s; Lipp and Niggli, 1993; Ishida et al., 1999) can have 3–4 orders of magnitude smaller wavelengths than macroscopic events of interest and can indeed be confined within a single cell. Because of the tight link between calcium and transmembrane voltage, such microscopic events might turn out to be of critical importance to understanding arrhythmias. Maintaining macroscopic FOV, and taking into account sub-cellular events, sets very high requirements for the spatial resolution of an ideal optical mapping system. Even if only two points (Nyquist) are sampled within a cell (along its shorter side), this demands spatial resolution of $\delta x_{max} = 10\,\mu m$ over an area $> 1\,cm$ (i.e. > 1000 pixels along each dimension). Choosing sub-cellular spatial

resolution might not be appropriate for tissue-level imaging, because of the resolution limit set by extensive light scattering. However, in cell monolayers, non-specific light contribution from scattering is considerably less, allowing us to explore cardiac wave dynamics with finer spatial resolution.

Overall, in the choice of an "ideal" optical mapping system, the available resources (Eq. (12)) rather than the system parameters, become a limiting factor. Requirements for fine spatial resolution are particularly demanding since they factor twice in the bandwidth required for 2D imaging. The resources, R, involve factors external to the optical system, such as the information storage capacity, IC (bytes), and the bandwidth, B (bytes/s). These are closely linked to parameters of the optical system—number of pixels, N, and maximum recordable time-frames, M. The theoretical DR (bit resolution of the detector), DR, is a scaling factor. IC and B impose real limits for ultra-high-resolution detectors, which operate at the maximum performance of current day computer technology, as discussed in Section 4:

$$R = \{\mathrm{IC}, B\}\begin{cases} \mathrm{IC} = \mathrm{DR}\, N^2 M, \\ B = \frac{\mathrm{DR}\, N^2}{\delta t}. \end{cases} \tag{12}$$

7.3. Current technology vs. the ideal mapping system

The parameter space of an ideal optical mapping system forms a polygon bounded by physical and rationally derived limits: $\{(\delta x_{\mathrm{phys}}, \delta t_{\mathrm{phys}}), (\delta x_{\max}, \delta t_{\mathrm{phys}}), (\delta x_{\mathrm{phys}}, \delta t_{\max}), (\delta x_{\max}, \delta t_{\max})\}$, Fig. 7. Having set specific requirements for the temporal and spatial resolution of the ideal mapping system, we can assess the potential of current technology to meet these requirements. To quantify how close is a current detector to the parameter space of an ideal optical mapping system, we use a measure—equivalent to the Euclidian distance in space. However, we do the calculations in 3D space–time, including two space dimensions and a time dimension, scaled for spatiotemporal events by the conduction velocity, as follows:

$$\begin{aligned} \Delta s &= 0, && (\delta x \leqslant \delta x_{\max}) \wedge (\delta t \leqslant \delta t_{\max}), \\ \Delta s &= \sqrt{2}(\delta x - \delta x_{\max}), && (\delta x > \delta x_{\max}) \wedge (\delta t \leqslant \delta t_{\max}), \\ \Delta s &= \theta(\delta t - \delta t_{\max}), && (\delta x \leqslant \delta x_{\max}) \wedge (\delta t > \delta t_{\max}), \\ \Delta s &= \sqrt{\theta^2(\delta t - \delta t_{\max})^2 + 2(\delta x - \delta x_{\max})^2}, && (\delta x > \delta x_{\max}) \wedge (\delta t > \delta t_{\max}). \end{aligned} \tag{13}$$

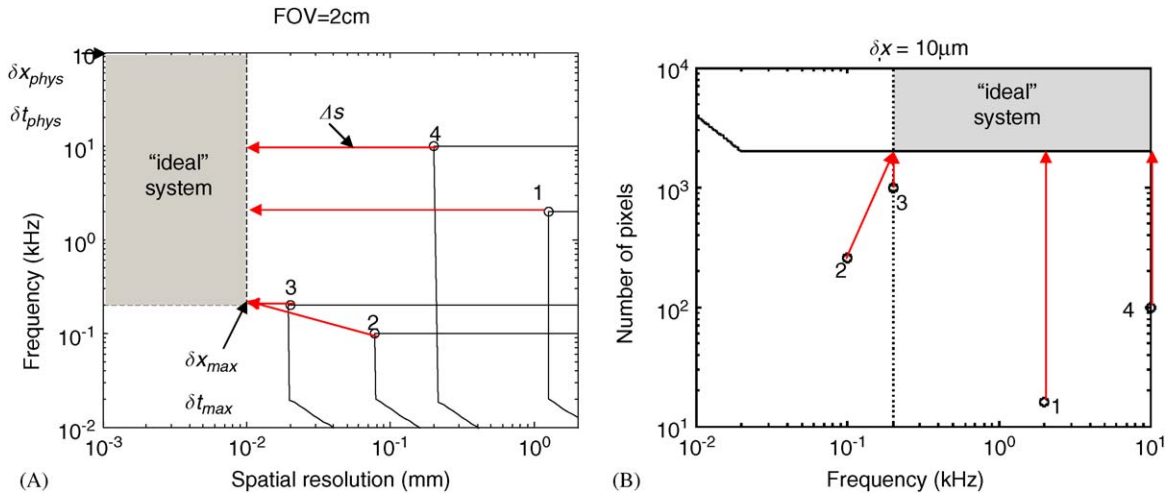

Fig. 7. Parameter space for an "ideal" optical mapping system (the gray box). (A) The spatial and temporal resolution of a system to image an FOV = 2 cm were considered here; the distance Δs for the four selected detectors from Fig. 6 is shown; (B) an alternative plane is shown (FOV and temporal resolution), under fixed 10 μm spatial resolution; the same four detectors are placed in this plane.

Fig. 8 presents some results for the shortest distance (Δs) from current detectors (Table 1) to the parameter space of two "ideal" systems—one with the already justified minimum requirements (200 Hz, 10 μm, left column) and another one with relaxed spatial resolution requirements but increased temporal resolution requirements (1 kHz, 50 μm, right column). The distance is measured according to Eq. (13), and presented in logarithmic format by color (white corresponds to $\Delta s = 0$). Six maps are shown, each is 12×6, where rows represent 12 detectors from Table 1, and columns represent six cases of maximum expected conduction velocity in the sample $\theta = \{5, 10, 20, 30, 40, 50\,\text{cm/s}\}$. As the size of the desired FOV to be mapped increases from 1 to 2 and 4 cm (top, middle and bottom), all detectors get further away from the ideal polygon, because of deterioration of their spatial resolution. At the same time, the effect of increasing expected conduction velocity in the sample affects most negatively the slow detectors (some CCD cameras), while PDAs are not affected by θ increase.

We present two examples of ultra-high-resolution imaging with an intensified camera system (pco CMOS 1280×1024), entry 12 in Table 1. After background subtraction and stretching the values at each pixel to the

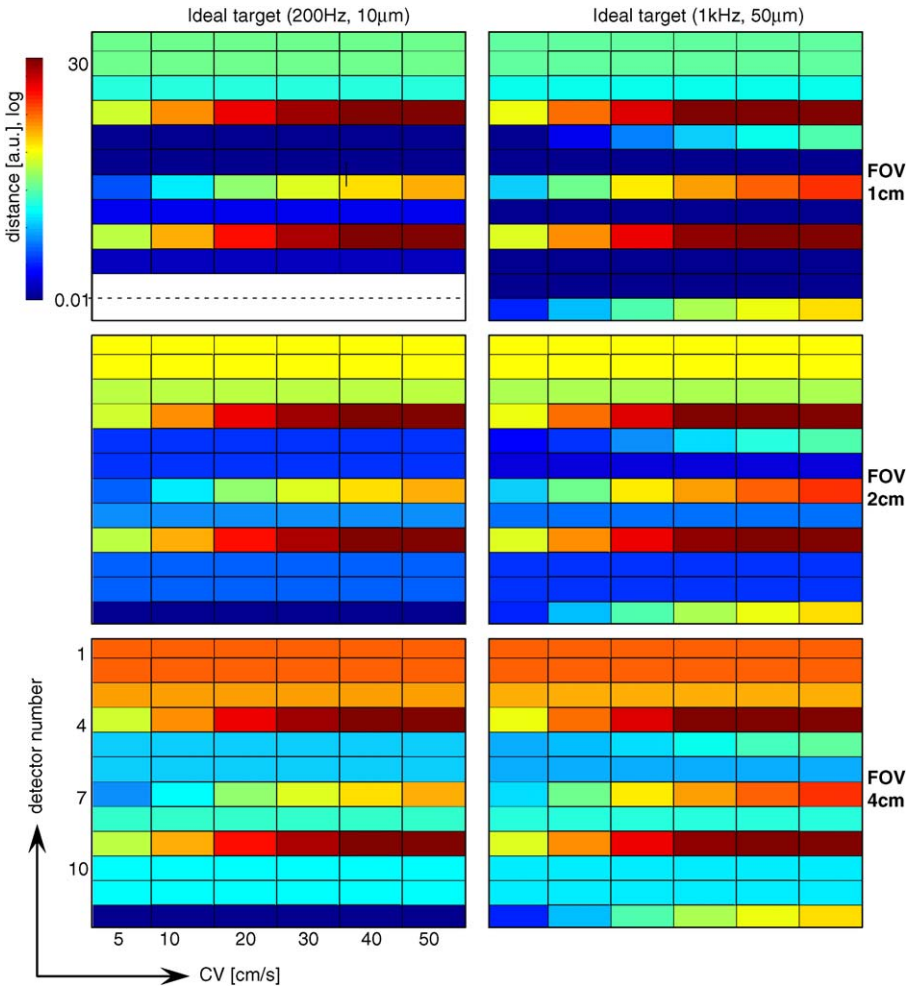

Fig. 8. Distance of current detectors from the "ideal" mapping system in the parameter space. The color represents distance from the "ideal" system as calculated by Eq. (13) (log 10 scale was used; white is zero distance). Each of the six images is a 12×6 matrix, where rows correspond to detectors 1–11 and 13 from Table 1, and columns represent six conduction velocities in the range 5–50 cm/s. Top, middle and bottom image rows correspond to FOV of 1, 2 and 4 cm, respectively. The left image column presents the distance of the selected detectors to an "ideal" system having a temporal resolution of 200 Hz and a spatial resolution of 10 μm; the right image column presents the distance of the selected detectors to a system with a temporal resolution of 1 kHz and a spatial resolution of 50 μm.

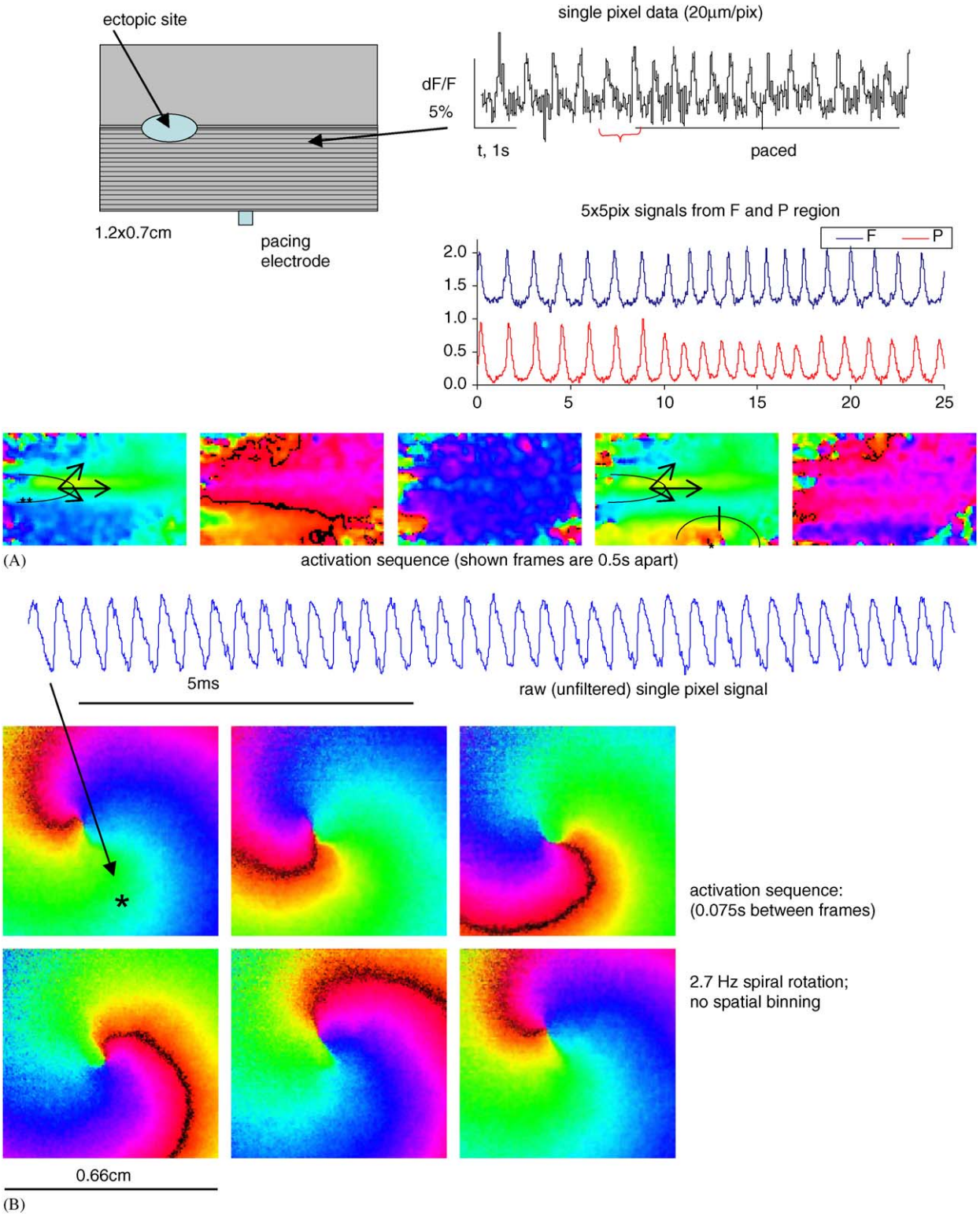

Fig. 9. Optical mapping with ultra-high spatiotemporal resolution in cell networks. (A) Transmembrane voltages (di-8-ANEPPS) were imaged (200 fps, 20 μm/pix) in a cell preparation grown on an elastic scaffold with a flat upper surface and a micro-grooved lower surface. Shown are temporal traces from a single pixel, and from 100 μm regions from the flat and peak portion. The phase color maps show the spontaneous activity from the border region (*), which was captured by point pacing from the lower border. (B) Spiral wave, rotating at 2.7 Hz, was imaged with Fluo-4 (200 fps, 20 μm/pix) in a cell monolayer. Raw (unfiltered) single pixel recording is shown from the periphery of the spiral (*), alongside equally spaced (0.075 s apart) spatial phase maps.

full DR, color maps of propagation were generated from the original images by converting intensity into phase values using the Hilbert transform (Bray and Wikswo, 2002); wavefront was tracked by a black line. No spatial or temporal filtering was applied. First, Fig. 9 presents macroscopic imaging in a single layer of cells at 200 fps and at 20 μm/pix within an FOV > 2 × 2 cm. We demonstrate that for both, calcium-sensitive dye

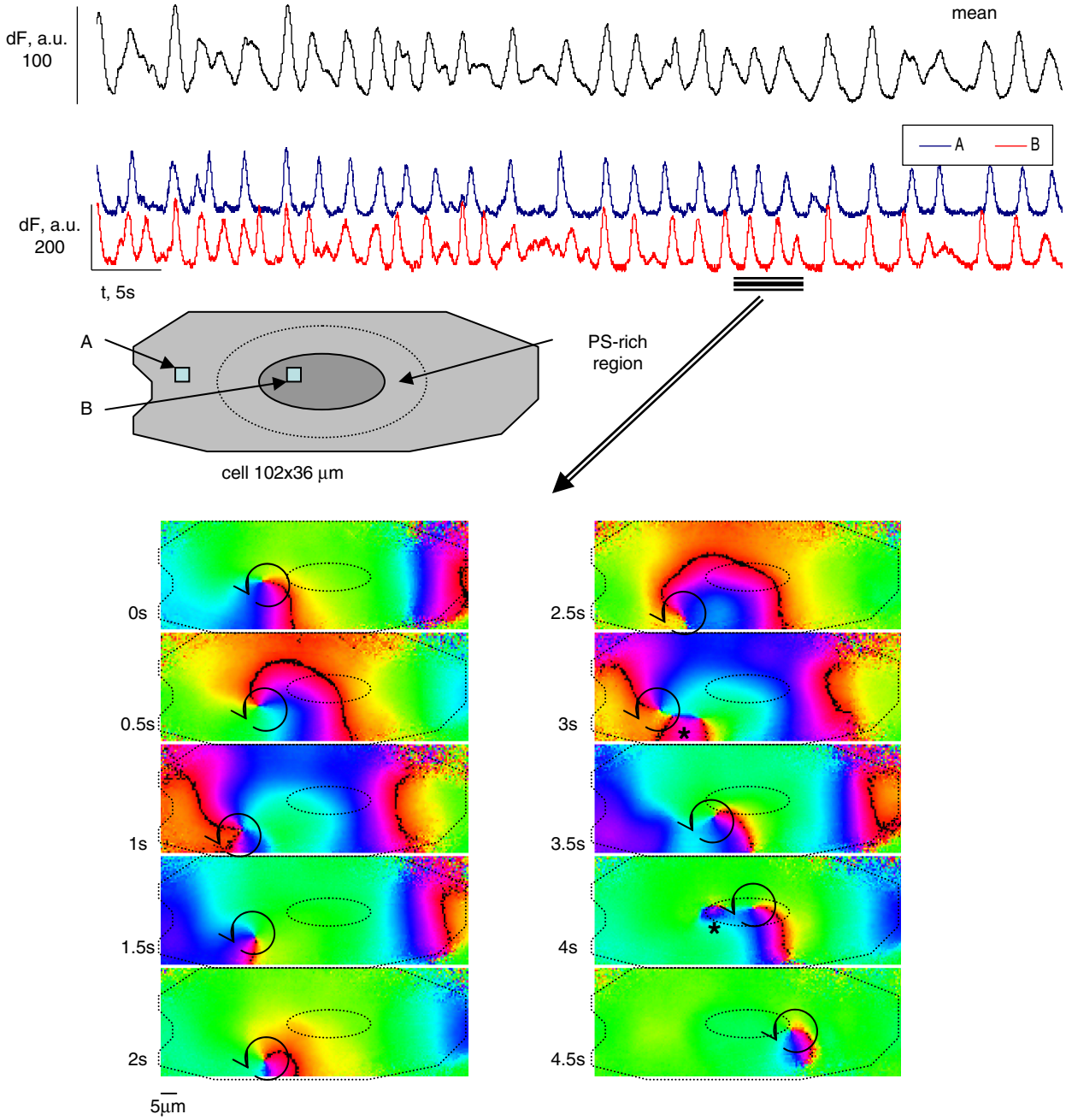

Fig. 10. Optical mapping with ultra-high spatiotemporal resolution in a single myocyte. Spontaneous intracellular calcium waves were mapped in a single mouse ventricular myocyte at 100 fps and 0.58 μm/pix. The mean fluorescence signal (Fluo-4) is shown (overall frequency 0.2 Hz), alongside selected single pixel raw data from the region inside and outside the nucleus. No spatial or temporal filtering was applied. Phase maps corresponding to selected 4.5 s of the recorded temporal sequence are presented. Most phase singularities (PS) were observed in the peri-nuclear region. A meandering spiral wave is shown in the maps; it gets displaced and subsequently eliminated by two target patterns (*), appearing at frames $t = 3$ and 4 s.

Fluo-4 and even voltage-sensitive dye di-8-ANEPPS, single pixel data (at 20 μm) are useful. At room temperature experiments, the speed of 200 fps is more than adequate to reveal details in cardiac propagation. Rigorous tests are needed to show whether this excessive spatial resolution (within a macro-FOV) compared to any previous imaging study reveals essential information not attainable in other mapping attempts. We believe that this mode of imaging brings together the two disparate scales of events (micro and macro, from sub-cellular to tissue level) in a way that is beneficial and indispensable for validating theoretically proposed arrhythmia mechanisms and guiding therapeutic strategies by uncovering previously not considered aspects.

Finally, Fig. 10, imaged by the same detector, but at 20 × micro-scale in a single murine myocyte stained with Fluo-4, was done at 100 fps and 0.58 μm/pix (at the optical limit of resolution). The peri-nuclear region of the cell was found to be rich of spiral waves accompanied by phase singularities, confirming some previous observations (Ishida et al., 1999). The example proves an important point that complexity of spatial patterns in cardiac propagation phenomena is preserved over a large range of spatial scales. For example, the core radius of a supported spiral wave at the macro- and micro-scale can change from 1000 μm down to 5 μm or less. This more than two orders of magnitude change in the spatial patterns emphasizes the importance and challenge to provide appropriate spatial resolution. Of course, the relevance of these micro-scale phenomena for arrhythmia genesis and maintenance remains to be confirmed.

8. Concluding remarks

The need for optical mapping at the micro- and macroscale simultaneously arises from the spatiotemporal complexity of excitation waves in the heart combined with our lack of full understanding and/or agreement which scale can safely be ignored when analyzing arrhythmias. The brute-force imaging approach solves this problem by imposing uniform requirements for ultra-high spatiotemporal resolution over a large FOV and a long recording period. The technical challenges associated with such solution and the expected performance of current day imaging technology was analyzed here; examples of optical recordings at ultra-high spatiotemporal resolution in cultured cells were also presented. The unprecedented data throughput challenges the current computer technology in terms of data acquisition and data storage. In addition, imaging at such ultra-high spatiotemporal resolution calls for development of specialized real-time data compression schemes and requires new ways to access, display and analyze the data, possibly exceeding the capabilities of current day 32 bit computer systems, including memory and file size limits. These software issues were not discussed in detail in this review, but are expected to become a central point in future imaging developments in this area.

If alternatively to the brute-force approach, two separate imaging systems are used to follow a "zoomed in" and "zoomed out" version of the excitation events, there still remains the need for dynamic positioning/focusing of the micro-mapping unit within the macroscopic FOV. A more intelligent design would require dynamic reconfiguring of the detector properties and non-uniform sampling to reduce the burden of excessive data generation and handling from regions outside of the zone(s) of interest. Theoretically, individual pixel addressability and control in the CMOS cameras, combined with the ultra-high inherent spatiotemporal resolution of these sensors may allow the implementation of this idea.

Optical imaging of excitation waves rides on cutting-edge technological innovations in the areas of imaging devices and electronics, optics, illumination, and computers; therefore, it is hard to predict the future system of choice. We presented here a theoretical framework for rational design of an imaging system based on the "shortest distance" to an "ideal" optical mapping system for a particular application. We offered a critical review of how is this choice influenced by the specific conditions and challenges encountered in imaging of cultured cell networks. The analysis is not limited to cardiac applications only, but is applicable to the dynamic imaging of any excitable cell system.

Acknowledgements

This work was supported in part by grants from The National Science Foundation (BES-0503336), The Whitaker Foundation (RG-02-0654) and the American Heart Association (0430307N) to EE, and a National Research Service Award to HB (1F30ES01337101).

References

Andor Technology, 2003. Making Sense of Sensitivity: Signal-to-Noise, Dynamic Range and Background Photons. Andor Technology. 〈www.andor.com〉.

Arutunyan, A., Webster, D.R., Swift, L.M., Sarvazyan, N., 2001. Localized injury in cardiomyocyte network: a new experimental model of ischemia-reperfusion arrhythmias. Am. J. Physiol. Heart Circ. Physiol. 280, 1905–1915.

Arutunyan, A., Swift, L.M., Sarvazyan, N., 2002. Initiation and propagation of ectopic waves: insights from an in vitro model of ischemia-reperfusion injury. Am. J. Physiol. Heart Circ. Physiol. 283, H741–H749.

Baxter, W.T., Davidenko, J.M., Loew, L.M., Wuskell, J.P., Jalife, J., 1997. Technical features of a CCD video camera system to record cardiac fluorescence data. Ann. Biomed. Eng. 25, 713–725.

Baxter, W.T., Mironov, S.F., Zaitsev, A.V., Jalife, J., Pertsov, A.M., 2001. Visualizing excitation waves inside cardiac muscle using transillumination. Biophys. J. 80, 516–530.

Berenfeld, O., Mandapati, R., Dixit, S., Skanes, A.C., Chen, J., Mansour, M., Jalife, J., 2000. Spatially distributed dominant excitation frequencies reveal hidden organization in atrial fibrillation in the Langendorff-perfused sheep heart. J. Cardiovasc. Electrophysiol. 11, 869–879.

Bien, H., Yin, L., Entcheva, E., 2003. Cardiac cell networks on elastic microgrooved scaffolds. IEEE Eng. Med. Biol. Mag. 22, 108–112.

Bray, M.A., Wikswo, J.P., 2002. Considerations in phase plane analysis for nonstationary reentrant cardiac behavior. Phys. Rev. E. Stat. Nonlin. Soft. Matter Phys. 65, 051902.

Bub, G., Glass, L., Publicover, N., Shrier, A., 1998. Bursting calcium rotors in cultured cardiac myocyte monolayers. Proc. Nat. Acad. Sci. USA 95, 10283–10287.

Bub, G., Shrier, A., Glass, L., 2002. Spiral wave generation in heterogeneous excitable media. Phys. Rev. Lett. 88, 058101.

Bub, G., Tateno, K., Shrier, A., Glass, L., 2003. Spontaneous initiation and termination of complex rhythms in cardiac cell culture. J. Cardiovasc. Electrophysiol. 14, S229–S236.

Bullen, A., Saggau, P., 1998. Indicators and optical configuration for simultaneous high-resolution recording of membrane potential and intracellular calcium using laser scanning microscopy. Pflugers Arch. 436, 788–796.

Bullen, A., Saggau, P., 1999. High-speed, random-access fluorescence microscopy: II. Fast quantitative measurements with voltage-sensitive dyes. Biophys. J. 76, 2272–2287.

Bullen, A., Saggau, P., Bullen, A., Patel, S.S., Saggau, P., 1997. High-speed, random-access fluorescence microscopy: I. High-resolution optical recording with voltage-sensitive dyes and ion indicators. Biophys. J. 73, 477–491.

Cabo, C., Pertsov, A.M., Baxter, W.T., Davidenko, J.M., Gray, R.A., Jalife, J., 1994. Wave-front curvature as a cause of slow conduction and block in isolated cardiac muscle. Circ. Res. 75, 1014–1028.

Cheng, H., Lederer, M.R., Lederer, W.J., Cannell, M.B., 1996. Calcium sparks and $[Ca^{2+}]i$ waves in cardiac myocytes. Am. J. Physiol. 270, C148–C159.

Cheung, J.Y., Tillotson, D.L., Yelamarty, R.V., Scaduto Jr., R.C., 1989. Cytosolic free calcium concentration in individual cardiac myocytes in primary culture. Am. J. Physiol. 256, C1120–C1130.

Choi, B.R., Salama, G., 2000. Simultaneous maps of optical action potentials and calcium transients in guinea-pig hearts: mechanisms underlying concordant alternans. J. Physiol. 529 (Part 1), 171–188.

Choi, B.R., Nho, W., Liu, T., Salama, G., 2002. Life span of ventricular fibrillation frequencies. Circ. Res. 91, 339–345.

Chudin, E., Goldhaber, J., Garfinkel, A., Weiss, J., Kogan, B., 1999. Intracellular Ca^{2+} dynamics and the stability of ventricular tachycardia. Biophys. J. 77, 2930–2941.

Cohen, L.B., Salzberg, B.M., Grinvald, A., 1978. Optical methods for monitoring neuron activity. Annu. Rev. Neurosci. 1, 171–182.

Denvir, D.J., Conroy, E., 2003. Electron Multiplying CCD Technology: the New ICCD. Andor Technology. 〈www.andor.com〉.

Domke, J., Parak, W.J., George, M., Gaub, H.E., Radmacher, M., 1999. Mapping the mechanical pulse of single cardiomyocytes with the atomic force microscope. Eur. Biophys. J. 28, 179–186.

Efimov, I.R., Nikolski, V.P., Salama, G., 2004. Optical imaging of the heart. Circ. Res. 95, 21–33.

Ehrenberg, B., Farkas, D.L., Fluhler, E.N., Lojewska, Z., Loew, L.M., 1987. Membrane potential induced by external electric field pulses can be followed with a potentiometric dye [published erratum appears in Biophys J 1987 Jul;52(1): following 141]. Biophys. J. 51, 833–837.

Eisner, D.A., Choi, H.S., Diaz, M.E., O'Neill, S.C., Trafford, A.W., 2000. Integrative analysis of calcium cycling in cardiac muscle. Circ. Res. 87, 1087–1094.

Entcheva, E., Lu, S.N., Troppman, R.H., Sharma, V., Tung, L., 2000. Contact fluorescence imaging of reentry in monolayers of cultured neonatal rat ventricular myocytes. J. Cardiovasc. Electrophysiol. 11, 665–676.

Entcheva, E., Bien, H., Yin, L., Chung, C.Y., Farrell, M., Kostov, Y., 2004a. Functional cardiac cell constructs on cellulose-based scaffolding. Biomaterials 25, 5753–5762.

Entcheva, E., Kostov, Y., Tchernev, E., Tung, L., 2004b. Fluorescence imaging of electrical activity in cardiac cells using an all-solid-state system. IEEE Trans. Biomed. Eng. 51, 333–341.

Fast, V.G., Ideker, R.E., 2000. Simultaneous optical mapping of transmembrane potential and intracellular calcium in myocyte cultures. J. Cardiovasc. Electrophysiol. 11, 547–556.

Fast, V., Kleber, A., 1993. Microscopic conduction in cultured strands of neonatal rat heart cells measured with voltage-sensitive dyes. Circ. Res. 73, 914–925.

Fast, V.G., Kleber, A.G., 1995a. Block of impulse propagation at an abrupt tissue expansion: evaluation of the critical strand diameter in 2- and 3-dimensional computer models. Cardiovasc. Res. 30, 449–459.

Fast, V.G., Kleber, A.G., 1995b. Cardiac tissue geometry as a determinant of unidirectional conduction block: assessment of microscopic excitation spread by optical mapping in patterned cell cultures and in a computer model. Cardiovasc. Res. 29, 697–707.

Fast, V.G., Kleber, A.G., 1997. Role of wavefront curvature in propagation of cardiac impulse. Cardiovasc. Res. 33, 258–271.

Fast, V., Rohr, S., Gillis, A., Kleber, A., 1998. Activation of cardiac tissue by extracellular electrical shocks. Formation of secondary sources at intercellular clefts in monolayers of cultured myocytes. Circ. Res. 82, 375–385.

Fast, V.G., Cheek, E.R., Pollard, A.E., Ideker, R.E., 2004. Effects of electrical shocks on Cai2+ and Vm in myocyte cultures. Circ. Res. 94, 1589–1597.

Frampton, J.E., Orchard, C.H., Boyett, M.R., 1991. Diastolic, systolic and sarcoplasmic reticulum [Ca^{2+}] during inotropic interventions in isolated rat myocytes. J. Physiol. Lond. 437, 351–375.

Gillis, A.M., Fast, V.G., Rohr, S., Kleber, A., 1996. Spatial changes in transmembrane potential during extracellular electric shocks in cultured monolayers of neonatal rat ventricular myocytes. Circ. Res. 79, 676–690.

Gillis, A.M., Fast, V.G., Rohr, S., Kleber, A.G., 2000. Mechanism of ventricular defibrillation : the role of tissue geometry in the changes in transmembrane potential in patterned myocyte cultures. Circulation 101, 2438–2445.

Girouard, S.D., Laurita, K., Rosenbaum, D., 1996. Unique properties of cardiac action potentials recorded with voltage-sensitive dyes. J. Cardiovasc. Electrophysiol. 7, 1024–1038.

Gray, R., Pertsov, A., Jalife, J., 1998. Spatial and temporal organization of cardiac fibrillation. Nature 392, 75–78.

Grinvald, A., Hildesheim, R., 2004. VSDI: a new era in functional imaging of cortical dynamics. Nat. Rev. Neurosci. 5, 874–885.

Grinvald, A., Salzberg, B.M., Cohen, L.B., 1977. Simultaneous recording from several neurones in an invertebrate central nervous system. Nature 268, 140–142.

Grinvald, A., Shoham, A., Shmuel, D., Glasser, D., Vanzetta, I., Shtoyerman, E., Slovin, A., Sterkin, A., Wijnbergen, C., Hildesheim, R., Aeieli, A., 2001. In-vivo Optical Imaging of Cortical Architecture and Dynamics. Springer, New York.

Gross, D., Loew, L.M., Webb, W.W., 1986. Optical imaging of cell membrane potential changes induced by applied electric fields. Biophys. J. 50, 339–348.

Grynkiewicz, G., Poenie, M., Tsien, R.Y., 1985a. A new generation of Ca^{2+} indicators with greatly improved fluorescence properties. J. Biol. Chem. 260, 3440–3450.

Grynkiewicz, G., Poenie, M., Tsien, R.Y., 1985b. A new generation of Ca^{2+} indicators with greatly improved fluorescence properties. J. Biol. Chem. 260, 3440–3450.

Guatimosim, S., Dilly, K., Santana, L.F., Saleet, J.M., Sobie, E.A., Lederer, W.J., 2002. Local $Ca^{(2+)}$ signaling and EC coupling in heart: Ca(2+) sparks and the regulation of the [Ca(2+)](i) transient. J. Mol. Cell Cardiol. 34, 941–950.

Hynecek, J., 2001. Impactron—a new solid state image intensifier. IEEE Trans. Electron Devices 48, 2238–2241.

Hynecek, J., Nishiwaki, T., 2003. Excess noise and other important characteristics of low light level imaging using charge multiplying CCDs. IEEE Trans. Electron Devices 50, 239–245.

Inoue, S., Spring, K.R., 1997. Video Microscopy. The Fundamentals. Plenum Publishing Corp., New York.

Intel Corporation, 2005. Disk Interface Technology: Quick Reference Guide. Intel Co. 〈http://www.intel.com/technology/serialATA/pdf/NP2108.pdf〉.

Iravanian, S., Nabutovsky, Y., Kong, C.R., Saha, S., Bursac, N., Tung, L., 2003. Functional Reentry in Cultured Monolayers of Neonatal Rat Cardiac Cells. Am. J. Physiol. Heart Circ. Physiol.

Ishida, H., Genka, C., Hirota, Y., Nakazawa, H., Barry, W.H., 1999. Formation of planar and spiral Ca^{2+} waves in isolated cardiac myocytes. Biophys. J. 77, 2114–2122.

Johnson, P.L., Smith, W., Baynham, T.C., Knisley, S.B., 1999. Errors caused by combination of Di-4 ANEPPS and Fluo3/4 for simultaneous measurements of transmembrane potentials and intracellular calcium. Ann. Biomed. Eng. 27, 563–571.

Jongsma, H.J., Wilders, R., 2000. Gap junctions in cardiovascular disease. Circ. Res. 86, 1193–1197.

Katz, R.H., Gibson, G.A., Patterson, D.A., 1989. Disk System Architectures for High-Performance Computing. Proc. IEEE 77, 1842–1858.

Knisley, S.B., 1995. Transmembrane voltage changes during unipolar stimulation of rabbit ventricle. Circ. Res. 77, 1229–1239.

Knisley, S., Hill, B., 1995. Effects of bipolar point and line stimulation in anisotropic rabbit epicardium: assessment of the critical radius of curvature for longitudinal block. IEEE Trans. Biomed. Eng. 42, 957–966.

Kong, W., Walcott, G.P., Smith, W.M., Johnson, P.L., Knisley, S.B., 2003. Emission ratiometry for simultaneous calcium and action potential measurements with coloaded dyes in rabbit hearts: reduction of motion and drift. J. Cardiovasc. Electrophysiol. 14, 76–82.

Kucera, J.P., Kleber, A.G., Rohr, S., 1998. Slow conduction in cardiac tissue, II. Effects of branching tissue geometry. Circ. Res. 83, 795–805.

Kurebayashi, N., Yamashita, H., Nakazato, Y., Daida, H., Ogawa, Y., 2004. Behavior of $Ca^{(2+)}$ waves in multicellular preparations from guinea pig ventricle. Am. J. Physiol. Cell Physiol. 287, C1646–C1656.

Lackowicz, J.R., 1999. Principles of Fluorescence Spectroscopy. Kluwer Academic/Plenum Publishers, New York, NY.

Laurita, K.R., Singal, A., 2001. Mapping action potentials and calcium transients simultaneously from the intact heart. Am. J. Physiol. Heart Circ. Physiol. 280, 2053–2060.

Lin, S.F., Abbas, R.A., Wikswo, J.P., 1997. High-resolution high-speed synchronous epifluorescence imaging of cardiac activation. Rev. Sci. Instrum. 68, 213–217.

Lipp, P., Niggli, E., 1993. Microscopic spiral waves reveal positive feedback in subcellular calcium signaling. Biophys. J. 65, 2272–2276.

Loew, L.M., Cohen, L.B., Dix, J., Fluhler, E.N., Montana, V., Salama, G., Wu, J.Y., 1992. A naphthyl analog of the aminostyryl pyridinium class of potentiometric membrane dyes shows consistent sensitivity in a variety of tissue, cell, and model membrane preparations. J. Membr. Biol. 130, 1–10.

LSI Logic Corporation, 2005. Storage Solutions and Adapters. LSI Logic Co. 〈http://www.lsilogic.com/products/storage_adapters/〉.

Molecular Expressions, 2005. Optical Microscopy Primer: Proximity-Focused Image Intensifiers. Molecular Expressions. 〈http://www.molecularexpressions.com/primer/digitalimaging/concepts/proximity.html〉.

Morad, M., Salama, G., 1979. Optical probes of membrane potential in heart muscle. J. Physiol. 292, 267–295.

Murphy, D.B., 2001. Fundamentals of Light Microscopy and Electronic Imaging. Wiley-Liss, New York.

National Semiconductor, 2005. Interface Products Selection Guide. National Semiconductor. 〈http://www.national.com/appinfo/lvds/files/interface_selguide.pdf〉.

Noujaim, S.F., Lucca, E., Munoz, V., Persaud, D., Berenfeld, O., Meijler, F.L., Jalife, J., 2004. From mouse to whale: a universal scaling relation for the PR Interval of the electrocardiogram of mammals. Circulation 110, 2802–2808.

Patterson, R.H., Gibson, G.A., Katz, R.H., 1988. A case for redundant arrays of inexpensive disks (RAID). In: ACM Conference on Management of Data (SIGMOD). ACM Press, Chicago, pp. 109–116.

PCI-SIG Group, 2005. PCI Bus Specifications. PCI-SIG Group. 〈http://www.pcisig.com/specifications/〉.

PULNix America, 2005. Specifications of the Camera Link Interface Standard for Digital Cameras and Frame Grabbers. PULNix America and other companies. 〈http://www.compumodules.com/pdf/CameraLinkOfficial.pdf〉.

Ratzlaff, E.H., Grinvald, A., 1991. A tandem-lens epifluorescence macroscope: hundred-fold brightness advantage for wide-field imaging. J. Neurosci. Meth. 36, 127–137.

Robbins, M.S., Hadwen, B.J., 2003. The noise performance of electron multiplying charge-coupled devices. IEEE Trans. Electron Devices 50, 1227–1232.

Rohr, S., Kucera, J.P., 1997. Involvement of the calcium inward current in cardiac impulse propagation: induction of unidirectional conduction block by nifedipine and reversal by Bay K 8644. Biophys. J. 72, 754–766.

Rohr, S., Kucera, J.P., 1998. Optical recording system based on a fiber optic image conduit: assessment of microscopic activation patterns in cardiac tissue. Biophys. J. 75, 1062–1075.

Rohr, S., Salzberg, B.M., 1994. Multiple site optical recording of transmembrane voltage (MSORTV) in patterned growth heart cell cultures: assessing electrical behavior, with microsecond resolution, on a cellular and subcellular scale. Biophys. J. 67, 1301–1315.

Rohr, S., Shoelly, D., Kleber, A.G., 1991. Patterned growth of neonatal rat heart cells in culture. Morphological and electrophysiological characteristics. Circ. Res. 68, 114–130.

Rohr, S., Kucera, J.P., Fast, V.G., Kleber, A.G., 1997. Paradoxical improvement of impulse conduction in cardiac tissue by cellular uncoupling. Science 275, 841–844.

Rohr, S., Kucera, J.P., Kleber, A.G., 1998. Slow conduction in cardiac tissue, I. Effects of a reduction of excitability versus a reduction of electrical coupling on microconduction. Circ. Res. 83, 781–794.

Ross, W.N., Salzberg, B.M., Cohen, L.B., Grinvald, A., Davila, H.V., Waggoner, A.S., Wang, C.H., 1977. Changes in absorption, fluorescence, dichroism, and birefringence in stained giant axons: optical measurement of membrane potential. J. Membr. Biol. 33, 141–183.

Sakai, T., Kamino, K., 2001. Optical mapping approaches to cardiac electrophysiological functions. Jpn. J. Physiol. 51, 1–18.

Salama, G., 1988. Optical measurements of transmembrane potential in heart. In: Loew, L.M. (Ed.), Spectroscopic Membrane Probes. CRC Press, Boca Raton, FL, pp. 137–199.

Salama, G., Morad, M., 1976. Merocyanine 540 as an optical probe of transmembrane electrical activity in the heart. Science 48, 485–487.

Salzberg, B.M., 1989. Optical recording of voltage changes in nerve terminals and in fine neuronal processes. Annu. Rev. Physiol. 51, 507–526.

Sharifov, O.F., Ideker, R.E., Fast, V.G., 2004. High-resolution optical mapping of intramural virtual electrodes in porcine left ventricular wall. Cardiovasc. Res. 64, 448–456.

Spach, M., Heidlage, J.F., 1995. The stochastic nature of cardiac propagation at a microscopic level. Electrical description of myocardial architecture and its application to conduction. Circ. Res. 76, 366–380.

Spach, M.S., Heidlage, J.F., Dolber, P.C., Barr, R.C., 1998. Extracellular discontinuities in cardiac muscle. Evidence for capillary effects on the action potential foot. Circ. Res. 83, 1144–1164.

Spach, M.S., Heidlage, J.F., Dolber, P.C., Barr, R.C., 2000. Electrophysiological effects of remodeling cardiac gap junctions and cell size: experimental and model studies of normal cardiac growth. Circ. Res. 86, 302–311.

Takahashi, A., Camacho, P., Lechleiter, J.D., Herman, B., 1999. Measurement of Intracellular Calcium. Physiol. Rev. 79, 1089–1125.

Tominaga, T., Tominaga, Y., Yamada, H., Matsumoto, G., Ichikawa, M., 2000. Quantification of optical signals with electrophysiological signals in neural activities of Di-4-ANEPPS stained rat hippocampal slices. J. Neurosci. Methods 102, 11–23.

Tominaga, T., Tominaga, Y., Ichikawa, M., 2001. Simultaneous multi-site recordings of neural activity with an inline multi-electrode array and optical measurement in rat hippocampal slices. Pflugers Arch. 443, 317–322.

Tsien, R.Y., 1983. Intracellular measurements of ion activities. Annu. Rev. Biophys. Bioeng. 12, 91–116.

Tung, L., Kleber, A.G., 2000. Virtual sources associated with linear and curved strands of cardiac cells. Am. J. Physiol. Heart Circ. Physiol. 279, 1579–1590.

Wilen, A., Schade, J.P., Thornburg, R., 2002. Introduction to PCI Express: a Hardware and Software Developer's Guide. Intel Press.

Windisch, H., Muller, W., Tritthart, H.A., 1985. Fluorescence monitoring of rapid changes in membrane potential in heart muscle. Biophys. J. 48, 877–884.

Winfree, A.T., 1998. A spatial scale factor for electrophysiological models of myocardium. Prog. Biophys. Mol. Biol. 69, 185–203.

Winfree, A., 1997. Heart muscle as a reaction-diffusion medium: the roles of electric potential diffusion, activation front curvature, and anisotropy. Int. J. Bifurc. Chaos. 7, 487–526.

Witkowski, F., Leon, L.J., Penkoske, P., Clark, G., Spano, M., Ditto, W., Giles, W., 1998a. A method for visualization of ventricular fibrillation: design of a cooled fiberoptically coupled image intensified CCD data acquisition system incorporating wavelet shrinkage based adaptive filtering. Chaos 8, 94–102.

Witkowski, F., Leon, L.J., Penkoske, P., Giles, W., Spano, M., Ditto, W., Winfree, A., 1998b. Spatiotemporal evolution of ventricular fibrillation. Nature 392, 78–82.

Wu, J.Y., Cohen, L.B., 1999. Optical measurement of membrane potential. In: Mason, W.T. (Ed.), Fluorescent and Luminescent Probes for Biological Activity: a Practical Guide to Technology for Quantitative Real-Time Analysis. Academic Press, San Diego, CA, pp. 389–404.

Wu, J.Y., Lam, Y.W., Falk, C.X., Cohen, L.B., Fang, J., Loew, L., Prechtl, J.C., Kleinfeld, D., Tsau, Y., 1998. Voltage-sensitive dyes for monitoring multineuronal activity in the intact central nervous system. Histochem. J. 30, 169–187.

Wu, T.J., Lin, S.F., Weiss, J.N., Ting, C.T., Chen, P.S., 2002. Two types of ventricular fibrillation in isolated rabbit hearts: importance of excitability and action potential duration restitution. Circulation 106, 1859–1866.

Yin, L., Bien, H., Entcheva, E., 2004. Scaffold topography alters intracellular calcium dynamics in cultured cardiomyocyte networks. Am. J. Physiol. Heart Circ. Physiol. 287, H1276–H1285.

Zaitsev, A.V., Berenfeld, O., Mironov, S.F., Jalife, J., Pertsov, A.M., 2000. Distribution of excitation frequencies on the epicardial and endocardial surfaces of fibrillating ventricular wall of the sheep heart [see comments]. Circ. Res. 86, 408–417.

Zwillinger, D., 1996. CRC: Standard Mathematical Tables and Formulae. CRC Press, Boca Raton, FL.